The optical, physical properties and direct radiative forcing of urban columnar aerosols in Yangtze River Delta, China

Bingliang Zhuang[1, *], Tijian Wang[1, **], Jane. Liu[1,2], Huizheng Che[3], Yong Han[1], Yu Fu[4], Shu Li[1], Min Xie[1], Mengmeng Li[1], Pulong Chen[1], Huimin Chen[1], Xiu-qun Yang[1], Jianning Sun[1]

[1] School of Atmospheric Sciences, CMA-NJU Joint Laboratory for Climate Prediction Studies, Jiangsu Collaborative Innovation Center for Climate Change, Nanjing University, Nanjing 210023, China

[2] Department of Geography and Planning, University of Toronto, Toronto, M5S 3G3, Canada

[3] Key Laboratory of Atmospheric Chemistry (LAC), Chinese Academy of Meteorological Sciences (CAMS), CMA, Beijing, 100081, China

[4] Dalian Weather Modification Office, Dalian, 116001, China

[*] Corresponding author, E-mail: blzhuang@nju.edu.cn; Tel.: +862589681156; fax: +862589683797

[* *]Corresponding author, E-mail: tjwang@nju.edu.cn; Tel.: +862589683797; fax: +862589683797

Abstract: The fractionated aerosol optical and physical properties as well as its direct radiative forcing (DRF) in urban area of west Yangtze River Delta (YRD) are investigated, based on the measurements of Cimel sun-photometer combined with a radiation transfer model. Ground based observed aerosols have much higher temporal resolutions compared with satellite retrievals. Analysis firstly reveals the characteristics of fractionated aerosol optical properties of different aerosol types in west YRD. The annual mean optical depth of the total aerosols is 0.65±0.28, dominated by the scattering aerosols (93.8%), with a mean refractive index of 1.44+0.0084i at 440 nm. The fine aerosols are about 4 times to, and also have very different compositions from the coarse ones. The absorbing components only account for ~4.6% in fine aerosols while 15.5% in coarse aerosols, but within the same mode, they have smaller sizes than scattering aerosols. Therefore, the fine particles are much scattering than the

coarse ones, simultaneously reflecting that each component has different size distributions. Relationships among the optical properties quantify the aerosol mixings and they imply about 15% and 27.5% occurrences of dust and black carbon dominated mixing aerosols, respectively, in west YRD. Different from optical properties, aerosols in west YRD have the similar volume size distributions to the ones in other sites over east China climatologically, peaking at the radius of 0.148 and 2.94 μm. But analysis further reveals that the fine or coarse dominated particles could individually lead to severe haze pollutions in YRD. Observed based estimations indicate that both the fine and coarse aerosols in west YRD exert a negative DRF, especially for the former one (-11.17 W/m^2 at the top of atmosphere, TOA). A higher absorption fraction directly leads to the negative DRF being offset more substantially for coarse aerosols (-0.33 W/m^2) at the TOA. Similarly, the coarse mode DRF only contributes to ~14% within scattering aerosols while >34% witnin absorbing aerosols. Sensitive analysis states that aerosol DRFs is not very sensitive to its profiles in clear sky condition. Both the aerosol properties and DRFs have substantial seasonality in west YRD. Results further reveal the contributions of each component in different size segments to the total AODs and DRFs. Also they are advantageous to improve the model performances on the aerosol and its effects in east regions of China.

1 Introduction

Atmospheric aerosols have significant influences on air quality, human health, and regional/global climate changes. Their loadings in the global atmosphere have increased substantially. Scientists suggested that the scattering aerosols could greatly offset the warming effects of greenhouse gases (Kiehl and Briegleb, 1993) while the absorbing components might further exacerbate the global warming (Jacobson 2002). The global mean direct radiative forcing (DRF) of scattering aerosols, fossil

47 fuel BC and the total aerosols was estimated to be about -0.55, +0.2, -1.04 W/m^2, respectively (Forster
48 et al., 2007; Reddy et al., 2005) at the top of atmosphere (TOA), thus changing the atmospheric
49 circulations and hydrological cycle. Menon et al. (2002) suggested that changes in the trend of rainfall
50 in China over the past 5 decades might be related to the variation of BC in Asia regions. Wang et al.
51 (2015) indicates that the East Asia summer monsoon circulation could become weaker due to the
52 cooling effects of the aerosols but stronger due to the warming effects of BC.

53 Although many studies on the aerosol radiative forcing and climate effects have been carried out
54 in both global and regional scales based on model simulations and observations in the past two decades
55 (e.g., Penner et al., 2001; Bellouin et al., 2003; Liao and Seinfeld, 2005; Wu et al., 2012; Wang et al.,
56 2015; etc.), large uncertainties still exist. Forster et al. (2007) pointed out that the global mean DRF
57 varied from +0.04 to -0.63 W/m^2 for the total aerosols and from +0.1 to +0.3 W/m^2 for BC. The ranges
58 were larger in regional scales, especially in high aerosol emitted regions (Zhuang et al., 2013a). The
59 DRF uncertainties would subsequently result in large bias of the aerosol climate effects. There are
60 many factors affecting the simulated radiative forcing, including the aerosol optical properties, which
61 are related to the aerosol emissions, size distributions, profiles, compositions, and mixing states (Holler
62 et al., 2003; Ma et al., 2017), surface albedo and clouds (Ma and Yu, 2012; Forster et al., 2007). The
63 uncertainties could be reduced substantially if the observed aerosol optical properties were figured out
64 and used (Forster et al., 2007).

65 With the rapid increase in population and growth in economics, the air pollutant emissions are
66 much higher in East Asia than in the other regions (Zhang et al., 2009). Additionally, dust aerosols from
67 desert regions are always transported to north and east China or even further afield (Wang et al., 2009;
68 Sun et al., 2012; Li et al., 2015a). Consequently, aerosols in China become frequently large in loadings

69 and complicated in compositions and spatial distributions (Zhang et al., 2012), especially in urban
70 agglomerations or megacities (e.g.: Yangtze River Delta: YRD). Therefore, it is necessary to clarify the
71 aerosol optical properties in YRD through observations, which is a premise for accurately estimating
72 the aerosol radiative effects and also in favor of improving the model performance on aerosols in east
73 region of China. Recently, substantial observation-based studies have conducted on both the surface
74 (e.g., Bergin et al., 2001; Xu et al., 2002; Zhang et al., 2004; Xia et al., 2007; Yan et al., 2008; He et al.,
75 2009; Fan et al., 2010; Cai et al., 2011; Xu et al., 2012; Wu et al., 2012; Zhang et al., 2015; Yu et al.,
76 2016; Deng et al., 2016; etc.) and columnar (e.g., Chiang et al., 2007; Pan et al., 2010; Yu et al., 2011;
77 Zhao et al., 2013; Tao et al., 2014; Zhu et al., 2014; Che et al., 2011; 2013; 2014; 2015a, b, c; Xia et al.,
78 2016; Zheng et al., 2016; Qi et al., 2016, etc.) aerosol optical properties (and DRFs), especially in
79 China. However, surface data could not completely represent the whole conditions of the aerosols in
80 atmosphere and they are highly affected by the variations of boundary layers. Its deficiency could be
81 made up by the measurements of the columnar aerosols. For the studies of surface aerosols, people
82 mainly focus on their absorption and scattering coefficients (AAC and SC). Investigations state that
83 both AACs and SCs in urban areas are frequently stronger than those at other sites. They were ~30 and
84 338 Mm^{-1} in west YRD (Zhuang et al., 2017). For columnar aerosol observations, the detailed aerosol
85 optical and physical properties could be obtained, including optical depth (AOD), refractive index,
86 Ångström exponents (AE), and so on. Che et al. (2015a) introduced a systematic long-term
87 measurement of the countrywide total aerosol AOD and AE in China from 2002 to 2013, and indicated
88 that annual mean AOD were 0.14, 0.74 and 0.54 at the rural sites, urban sites, and in east China,
89 respectively. In YRD, Pan et al. (2010) shows that AOD at 440 nm and AE in coastal area (east YRD)
90 was about 0.74 and 1.27, respectively. Yu et al. (2011) and Qi et al. (2016) indicate that the total aerosol

AOD exceeded 0.6 and its single scattering albedo (SSA) was ~0.88 in lake and urban areas of central to east YRD. Zhuang et al. (2014a) indicates that a one-year observed AOD and AE of the total aerosols in urban area of Nanjing (urNJ, west YRD) was similar to Pan et al. (2010), but difference existed. In addition to aerosol optical properties, the observed based aerosol DRFs are also estimated around the world (such as: Markowicz et al., 2008; Khatri et al., 2009; Kuhlmann and Quaas, 2010; Alam et al., 2011, Zhuang et al., 2014a, and Xia et al., 2016). However, almost all of their investigations focused on the total aerosol forcing. For example, Xia et al. (2016) stated that regional mean aerosol DRF in China was about -16~-37 W/m^2 at the TOA and about -66 ~ -111 W/m^2 at the surface when solar zenith angle was about 60^o.

Although considerable studies on the observed columnar aerosol optical properties have been carried out in China or even within YRD (one of the rapidest urbanization regions in China), there still have gaps need to be improved for the current observations, especially in the urban areas of the region with intense human activities. In YRD or east China, most of the investigations on the aerosol optical properties were focused on the coast, lake and rural regions (Pan et al., 2010; Yu et al., 2011; Che et al., 2015a; Qi et al., 2016) of central to east YRD. And most of them only address the total aerosol optical properties (independent of modes and compositions) except Qi et al., (2016), who also made an introduction on the aerosol physical parameters and size fractional SSA in eastern coast city (Hangzhou, hereinafter short for urHZ) of YRD. There is about 300 km of urHZ away from west YRD. As implied in Zhang et al. (2012), aerosols are complicated in compositions and spatial distributions especially in fast developing regions (such as YRD). Thus, large differences of the aerosol optical and physical properties might exist to degrees among the sites within YRD. Additionally, none of researches mentioned above have studied the aerosol DRFs. Some investigations on the columnar aerosols in west

YRD (urNJ) have been carried out in Zhuang et al. (2014a), but significant issues (not considered in theirs) still need to be further addressed, such as the size fractional optical parameters and DRFs of different aerosol components, as well as the size fractional aerosol physical properties. Therefore, it's still necessary to make a more integrated investigation on the aerosol optical and physical properties, as well as their DRFs in YRD. In this study, the unaddressed issues in west or whole YRD region mentioned above will be all included based on the measurements of Cimel sun-photometer in urNJ, combined with a radiation transfer model (TUV, Madronich, 1993). Additionally, the aerosol types and mixings in the region will be further identified and discussed based on the relationships among the aerosol optical properties. Third, the observed aerosol profiles, which have not been considered before in YRD, are further used and discussed here to calculate the aerosol DRFs. It believes that the results here would be advantageous to further understand the characteristics of aerosols over east region of China. Also, they are helpful to improve the model performance on the aerosol and its climate effects in relevant regions. Because, first of all, the observed aerosol parameters could be used for data assimilation to obtain more accurate inputs (including initial conditions and air pollutant emissions) of the model (Jiang et al., 2013 and Peng et al., 2017). Second, a more precise aerosol refractive index and size distribution used in numerical models would yield a more reasonable aerosol loadings and DRFs (Ma et al., 2017). Third, both the aerosol optical properties and DRFs could be used to validate the simulations.

The method is described in Section 2. Results and discussions are presented in Section 3, followed by Conclusions in Section 4.

2 Methodologies

2.1 Sampling station and instruments

The observation site (Urban Environmental Monitoring Station of Nanjing University) is located in the downtown area of Nanjing City (hereinafter short for urNJ, 32.05^{o} N, 118.78^{o} E), west YRD. It is built on the roof of a 79.3 m-tall building, around which there almost have no higher obstacles and no industrial pollution sources within a 30 km radius but there are several main roads with apparent traffic pollutions. Detailed information of the site is available in Zhu et al. (2012).

The columnar aerosol optical properties and physical characters at the site were from measurements of the Cimel sun photometer (CE-318, Holben et al., 1998) during the period from Apr 2011 to Feb 2014. Routine maintains and calibrations were made during the observation period. Due to the malfunctions of the instrument and the problems of data transmission, the data from May to Sep 2012 and from Aug to Dec 2013 are invalid and excluded. The wavelength dependent optical depth (AOD) and Ångström exponents (AE) of the total aerosols were directly measured by CE-318, while the following variables, including the aerosol size distributions, fractionated (fine and coarse) aerosol effective radius (R_{eff}), mean radius (R_{mn}), volume concentrations (Vol), wavelength dependent size fractional optical depth of the scattering, absorbing and total aerosols, aerosol single scattering albedo (SSA), as well as wavelength dependent refractive indices, are derived from the DOBVIC algorithm Version 2 (Dubovik et al., 2000; 2006). This algorithm has been widely used by the Aerosol Robotic Network (AERONET) and the China Aerosol Remote Sensing Network (CARSNET) and the products have been used globally as introduced in Introduction due to their high accuracies. The errors for AOD, absorption AOD (AAOD), SSA is 0.01, 0.01 and 0.03, respectively (Yu et al., 2011; Li et al., 2015c). The errors of the fine and coarse aerosol SSA is 0.037 and 0.085, respectively (Xu, 2015). The error of the refractive index is 0.04 for real part and 0.0025-0.0042 for imaginary part (Yu et al., 2011). And the

error of the volume size distribution is less than 10% in peak regions while about 35% in valley region or interval region between fine and coarse modes (Yu et al., 2011). Detailed descriptions on CE-318 and the corresponding observations in CARSNET are available in Li et al. (2015a) and Che et al. (2015a). For comparison, 550 nm AODs and SSAs are calculated based on given AODs at other wavelengths and AEs (Angstrom. 1929):

$$AOD_{550nm} = AOD_{440nm} \times (\frac{550_{nm}}{440_{nm}})^{-AE_{440/870nm}} \quad (1)$$

$$AAOD_{550nm} = AAOD_{440nm} \times (\frac{550_{nm}}{440_{nm}})^{-AAE_{440/870nm}} \quad (2)$$

$$SSA_{550nm} = \frac{AOD_{550nm} - AAOD_{550nm}}{AOD_{550nm}} \quad . \quad (3)$$

To make a further comparison, the concurrent observations of surface total aerosol absorption coefficient (AAC) and Ångström exponents (AAE) measured by a 7-channel Aethalometer (model AE-31, Magee Scientific, USA, Hansen et al., 1984; Weingartner et al., 2003 and Arnott et al., 2005) are used. Detailed calculation and correction of AAC at the site could be found in Zhuang et al. (2015). In addition, monthly mean optical depth (AOD) and Ångström exponent (AE) of the total aerosols from satellite of Moderate Resolution Imaging Spectroradiometer (MODIS) were used to assist the analysis.

Based on observed wavelength dependent aerosol optical properties, the aerosol direct radiative forcing (DRF) in urNJ is investigated using a radiation transfer model TUV (Madronich, 1993). Only clear sky DRFs are addressed here because almost all of the measurements are carried out in free sky condition. The solar component of the radiative transfer scheme in TUV follows the δ-Eddington approximation. In addition to the aerosol optical properties, surface alebdo (Palancar and Toselli, 2004) and the aerosol vertical profiles (Forster et al., 2007) might also have significant influences on DRF.

Thus, the wavelength dependent surface albedo from MODIS, the annual and seasonal mean aerosol profiles from Cloud-Aerosol Lidar and Infrared Pathfinder Satellite Observations (CALIPSO) and Polarization-Raman Lidar in Nanjing would be included when assessing the aerosol DRF. The aerosol DRF in this study is defined as the difference in net shortwave radiative fluxes between including and excluding aerosol effects at the TOA and surface. Gas absorptions in the atmosphere were set to be constant. The scattering aerosol's SSA was set to 0.9999 (similar to sulfate or nitrate, Li et al., 2015b) when calculating its DRF. DRF of the absorbing aerosols is derived from the differences between the total and the scattering aerosol DRFs.

3 Results and discussions

3.1 Optical properties of the aerosols

In this section, 550 nm optical depth, single scattering albedo and 440 nm refractive indices of the aerosols are discussed as representatives for the temporal variations and frequency distributions of these three kinds of the aerosol optical parameters. In addition to the whole mode aerosols, the size fractional (fine and coarse ones) aerosol optical properties of different components (scattering and absorbing aerosols) are also discussed in this section. Therefore, there are altogether nine types of aerosols, including the total aerosols, total fine aerosols, total coarse aerosols, scattering aerosols, fine scattering aerosols, coarse scattering aerosols, absorbing aerosols, fine absorbing aerosols, and coarse absorbing aerosols.

Table 1 summary the statistics of the aerosol optical properties during the study period in urNJ. The mean 550 nm optical depth (AOD) of the total aerosols is 0.65, and the scattering aerosols account for as large as about 94%. Fine mode aerosol AODs (FAOD, FSAOD and FAAOD) accounts for

81.53%, 81.97% and 56.09% of the total AOD, scattering AOD (SAOD) and absorbing AOD (AAOD) in this wavelength, respectively, implying that coarse aerosols is more absorbing than the fine ones. 440/870 nm AE of the total, scattering and absorbing aerosols are about 1.20, 1.19, and 1.32, respectively. Fine aerosols have much larger AEs, 0.4-0.5 larger than the total aerosols. Overall, the absorbing aerosols have smaller sizes than the scattering ones in all modes, especially in coarse mode, which is consistent with the results of the surface aerosols at the site (Zhuang et al., 2017). Annual mean 470/660 AAE (from AE-31) and 450/635 nm SAE (from Nephelometer Model Aurora 3000) of the near surface aerosols are 1.58 and 1.32, respectively, at the site during the period from March 2014 to Feb 2016 (Zhuang et al., 2017). The mean 550 nm SSAs are 0.93, 0.95 and 0.82 for the total, fine and coarse aerosols, respectively, further implying that the coarse aerosols have different compositions and have much stronger ability to absorb solar short wave radiation than the fine aerosols. Comparisons also indicate that surface aerosol (SSA=0.9 in Zhuang et al., 2017) is a little more absorption than the columnar aerosols in urNJ. Annual mean surface SSA at 550 nm for the total aerosols is little smaller (0.9) than the column one. The mean 440 nm refractive index is about 1.44+0.0084i. The table also implies that west YRD could suffer very serious particle pollutions.

Table 1

3.1.1 Seasonal variations of the aerosol optical properties

Figure 1 presents the monthly variations of 550 nm AOD (a), SAOD (b) and AAOD (c) as well as the contributions of their fine or coarse mode to the corresponding totals. Temporal variations of the total aerosol AOD is consistent with SAOD due to significantly large ratio of SAOD/AOD. AODs are all considerably high in winter due to a more intense emission of the trace gases and particles (Zhang et

222 al., 2009). However, a long distance transported dust aerosols from north China in spring and high
223 efficiencies of moisture absorption and scattering aerosol chemical transformation in summer (Li et al.,
224 2015a) also lead to high AODs in these two seasons. Therefore, dust episodes, relative humidity (RH)
225 and chemical processes weaken the seasonal variation of total AOD purely induced by the emissions in
226 urNJ, west YRD. Instead, these processes prominent the AOD seasonality of different aerosol types in
227 different size segments. The largest AODs appear in spring for coarse scattering and absorbing aerosols
228 while in summer for the fine ones in urNJ. The figure also implies that the scattering aerosols might
229 have different size distribution from the absorbing aerosols. The fine mode fraction rate is 0.83
230 (peaking at 0.97) for scattering aerosol while 0.56 (peaking at 0.83) for absorbing aerosol. In other
231 words, the fine aerosols have different compositions from the coarse ones.
232
233 Figure 1
234
235 The aerosol Ångström exponents also have substantially seasonal variations, especially for the
236 absorbing aerosols as illustrated in Figure 2. For each component (scattering or absorbing one), the
237 seasonal variations of its fine and coarse AEs are well agree with each other, all being close to zero line
238 in summer possibly due to the effects of high relative humidity (Zhuang et al., 2014a). The whole mode
239 AE of each aerosol type is determined by the both variations of AE in each mode and fine mode
240 fraction. Therefore, the smallest AE appears in summer (0.74 in July) for the total absorbing aerosols
241 while in spring (0.94 in Mar) for the total scattering aerosols. Similarly, the total aerosol AE is
242 determined by the both variations of each aerosol type's AE and fraction rate of the scattering (or
243 absorbing) aerosol to the totals. Similar to AOD, the seasonality of the total aerosol AEs is more

consistent with that of the scattering aerosols. The figure also indicates that the scattering aerosols have much larger sizes than the absorbing aerosols, especially in coarse mode. Further comparison indicates that the seasonal variations of columnar SAE and AAE are consistent with the ones of surface SAE and AAE (results not shown here) at the site.

Figure 2

In addition to AOD and AE, monthly variations of the aerosol single scattering albedo (SSA) and refractive indices are also investigated as shown in Figure 3. SSA is affected by both scattering and absorbing aerosols, as well as their relative contributions. The fine particles are much more scattering than the coarse aerosols. However, the coarse aerosol SSA has more significant seasonality. Overall, both FSSA and CSSA are relative smaller in summer than in the other seasons although they are considerable large in August 2011, implying that the two types of aerosols in summer are more absorbing than in the other seasons. The total aerosol SSA is somewhere in between FSSA and CSSA depending on the ratios of FAOD to AOD and it has different seasonal variation from FSSA or CSSA. SSA is the smallest in spring due to the largest contribution of coarse aerosols. The aerosol refractive indices also show substantial seasonality. The real part is large in spring but small in summer, which is similar to what was observed in Taihu Lake in central YRD (Yu et al. 2011). The imaginary parts show relatively weaker seasonal variations than the real parts.

Figure 3

Table 2 summarizes the abovementioned seasonal means with the corresponding standard deviations for the all aerosol optical properties. It provides more quantitative variations of the aerosol optical properties compared with the figures above. Seasonal mean 550 nm AOD, SAOD and AAOD vary from 0.59 in fall to 0.75 in summer, from 0.55 in fall to 0.70 in summer, and from 0.037 in fall to 0.050 in spring, respectively. CAOD, CSAOD, CAAOD account for the majority of AOD, SAOD and AAOD in spring, with the ratios of 30.1%, 27.9%, and 58.1%, respectively. FAOD, FSAOD, FAAOD account for the majority of AOD, SAOD and AAOD in summer, with the ratios of 90.5%, 91.2% and 70.2%, respectively. As discussed above, the seasonal variations of the total mode aerosol AEs and SSA are different from the ones in each mode. The seasonal mean 440/870 nm SAE and AAE vary from 0.98 in spring to 1.38 in fall, and from 0.78 in summer to 1.50 in winter. Seasonal mean FSSA and CSSA vary from 0.940 in summer to 0.956 in winter and from 0.787 in summer to 0.834 in spring, respectively. The real part of the aerosol refractive index has relatively stronger seasonality than the imaginary part. Their largest values are all found in spring. Comparisons indicate that the seasonal variation of the optical properties is highly inhomogeneous spatially within YRD. As indicated in Che et al. (2015a) and Qi et al. (2016), the largest AOD was found in spring while the lowest one appeared in summer in urHZ, another city in eastern coast of YRD. In Taihu Lake, a rural site in central YRD, the lowest AOD appeared in winter (Pan et al., 2010; Yu et al., 2011). Additionally, the aerosols are the most absorbing in winter in central regions of YRD (Taihu Lake and urHZ) and their SSA are as small as 0.88 (Yu et al., 2011 and Qi et al., 2016). Aerosols in west YRD (urNJ) are more scattering than theirs and the smallest SSA appears in spring during the sampling periods. Nevertheless, AE variations are more consistency with each other among these sites, being smallest in spring and largest in fall.

Table 2

288

289 **3.1.2 Frequencies of the aerosol optical properties**

290 All AODs and SSAs follow a near lognormal pattern and almost all of the AE and refractive
291 indices follow a unimodal pattern (Figure 4). The ranges around their means dominated, accounting for
292 at least 60% to their total data samples during the entire study period. Similar to the temporal variation,
293 frequency distributions of the total aerosols (not shown) are also highly similar to the ones of scattering
294 aerosols in both fine and coarse modes.

295 The frequencies of the absorbing aerosol AEs are different from the scattering ones, so is FAAE
296 and CAAE. The occurrences of smaller CAAE are relatively high. However, the large FAAE exceeding
297 2.5 also has contributions (more than 5.4%). Both fine and coarse absorbing aerosols have much
298 smaller sizes than the scattering aerosols at the same modes. Frequency distribution of SSA also
299 implies that the coarse aerosols are more absorbing than the fine aerosols. Consequently, the
300 frequencies of SSAs peak between 0.95 and 0.97, and between 0.80 and 0.84 for the fine and coarse
301 mode aerosols, respectively, in urNJ during the study period. Fine aerosol SSAs concentrates more in a
302 narrow range (from 0.89 to 0.99) than CSSA (from 0.64 to 0.96). For the refractive index, the
303 frequencies peak between 1.39 and 1.42, and between 0.007 and 0.009 for the real and imaginary parts,
304 respectively, in urNJ during the study period.

305 The frequency patterns of the aerosol optical properties also have substantial seasonality (not
306 shown here). Overall, the curves would shift left-ward in low value seasons and right-ward in high
307 value seasons. In summer, the AOD curves might even have two peaks for the scattering or total
308 aerosols, which are similar to the observations in Taihu Lake (Yu et al., 2011). For SAE, the peak shifts
309 left-ward in spring by 0.2, but right-ward in fall by 0.2. For SSA, both fine and coarse aerosol SSA

310 frequencies have a left-ward shift in summer compared to the annual one, which is opposite to the
311 frequency of the total SSA because the fine aerosol AODs dominate, accounting for about 91% of the
312 totals. The real part frequency in spring has a significant right-ward shift compared to that in the entire
313 study period, peaking between 1.46 and 1.50 (not shown). The imaginary part frequency in winter has a
314 significant left-ward shift compared to that in the study period, peaking between 0.001 and 0.003 (not
315 shown).
316
317 **3.1.3 Comparisons with MODIS AOD, AE and surface aerosols**
318 AOD and AE observed by CE-318 are in reasonable agreement with those from MODIS in
319 seasonal variation and magnitude (Figure 5). The linear correlation coefficients are 0.75 and 0.86
320 between CE-318 AOD and MODIS AOD and between CE-318 AE and MODIS AE, respectively. AOD
321 at 550 nm from MODIS is larger than from CE-318, with an average value of 0.82 during the study
322 period. The mean AE at 412/470 nm is about 1.43. The standard deviations of the AOD and AE are
323 much larger from CE-318 than from MODIS possibly due to a higher temporal resolution of CE-318
324 observations.
325
326 Figure 5
327
328 The columnar AAOD and AAE from CE-318 are fairly related to the surface aerosol absorption
329 coefficient (AAC) and AAE from AE-31 (Figure 6). However, the relationship between AAOD and
330 AAC or between column and surface AAEs is worse than that between CE-318's and MODIS'.
331 Although surface aerosols could be affected by transport, it is mainly from local and regional emissions

and its loadings are highly related to the degree of the boundary layer development. As suggested by Zhuang et al. (2014b and 2015), surface aerosol loadings are considerably low in afternoon and summer times when the boundary layer are well developed. The columnar AAOD could additionally be affected by the emissions and transportations in the upper atmosphere and it is less affected by the boundary height compared with the surface AAC, thus contributing a relatively worse relationship between AAOD and AAC. The surface AAE is more concentrated in a narrow range and it is larger (1.6) than that from CE-318, implying that the surface absorbing aerosols are finer and fresher. The linear correlation coefficients are 0.39 and 0.41 between AAOD and AAC and between columnar and surface AAEs, which is slightly worse than those between FAAOD and AAC (0.46) and between columnar FAAE and surface AAE (0.47).

Figure 6

3.1.4 Briefly discussions

Ground based observed aerosols have much higher temporal resolutions compared with satellite retrievals. The observed columnar optical properties could make up the deficiency of surface aerosol data on one hand, and make us better understand the characteristics of the aerosols on the other hand. Additionally, they might be useful for improving the model performances on the aerosols and their radiative effects in YRD or east China. The observed aerosol parameters could be used for data assimilation, which can produce more accurate initial conditions of the model and variations of the aerosol emissions (Jiang et al., 2013 and Peng et al., 2017). The data set of the optical properties in most of the climate or air quality models are frequently from a given refractive index which is

354 homogeneous in time and space. Therefore, a more precise aerosol refractive index used in numerical
355 models would yield a more reasonable aerosol optical properties and radiative forcing in observed
356 regions and around. Further, the observed aerosol optical properties could be also used to validate the
357 simulations.

358 As mentioned in Introduction, most studies on the aerosol optical properties in China mainly focus
359 on AOD and AE of the total aerosols in short term (i.e., episodes, Che et al., 2013; Zheng et al., 2016;
360 Che et al., 2015b). Studies on annual (Yu et al., 2011) and decadal (Che et al., 2015a) scales have been
361 carried out in recent years based on CE-318 measurements. Che et al. (2015a) indicated that long tern
362 averages of the total aerosol AOD at 440 nm and AE at 440/870 nm in urban areas were about 0.75 and
363 1.05 in north China, 0.98 and 1.09 in Sichuan Basin, 0.78 and 1.36 in Pearl River Delta region (PRD),
364 0.65 and 1.0 in northeast China, 0.66 and 89 in northwest China, 0.92 and 1.0 in central China, 0.9 and
365 1.25 in coastal areas of YRD. The mean AOD at 440 nm in urNJ is larger (0.84) than that in northern
366 China and PRD but smaller than that in coastal cities of YRD. Aerosols in northern and central China
367 have larger sizes (smaller AE) than those in west YRD. Che et al. (2015a) further suggested that the
368 aerosols in urban areas likely had larger AODs and AEs than those in mountain and desert areas, so did
369 in urNJ. Qi et al. (2016) presents that the aerosol single scattering albedo at 440 nm in urHZ is about
370 0.90, 0.92 and 0.70 for the total, fine and coarse aerosols, respectively, also implying that the coarse
371 aerosols are more absorbing than the fine ones. Our measurements show similar results to theirs.
372 However, aerosols in urNJ are more scattering than in urHZ in both fine and coarse modes, revealing
373 inhomogeneous distributions of the aerosol compositions in YRD. Although some studies on the
374 columnar aerosol optical properties based observations have been carried out in YRD (Pan et al., 2010;
375 Yu et al., 2011; Zhuang et al., 2014a; Che et al., 2015a, Qi et al., 2016), study here further fill the gaps

376 of the current observations. Based on authors previous research (Zhuang et al., 2014a), a more
377 comprehensive and systematic analysis on the fractionated optical properties of different aerosols types
378 are additionally carried out here. The results would be advantageous to further understand the aerosols
379 over east China.
380
381 **3.2 Physical properties of the aerosols**
382 In addition to the optical properties, the aerosol physical properties including volume size
383 distributions, mode dependent sizes (radius) and volume concentrations are also retrieved. Figure 7
384 shows the volume size distributions of the aerosols in different seasons (Figure 7a) and in different
385 AOD (or polluted) levels (Figure 7b) in urNJ. The figure shows that aerosols in urNJ have a typical
386 bimodal structure in volume size distribution in all seasons, presenting a two-mode lognormal
387 distribution: fine (radius < 0.6 μm) and coarse mode (radius > 0.6 μm). Their annual peaks appear at
388 the radius of 0.148 μm in fine mode and 2.94 μm in coarse mode. Similar to the aerosol optical
389 properties, aerosol volume size distribution also has substantial seasonality. Dust episodes lead to the
390 peak value in spring being much smaller in fine mode than in coarse mode, which is opposite to that in
391 the other seasons (especially in summer). Therefore, the mean radius of the aerosols increases
392 significantly in spring due to a high proportion of coarse particles, leading to a smaller AE as discussed
393 in precious sections. In summer, the curve has a right-ward shift, showing a larger aerosol size in both
394 fine and coarse modes due to high hygroscopic growth efficiency. The fine particles dominate in
395 summer and result in large AE, opposite to what is in spring. The aerosol volume size distribution
396 varies with different AOD values (Figure 7b) in urNJ. Overall, the peak value has a substantial
397 right-ward shift with increasing AOD for fine aerosols while a slightly left-ward shift for coarse

aerosols, implying that the growth of the fine aerosols is advantageous to enhance the aerosol radiative effect. In urNJ, both fine and coarse particles basically have the same levels when AOD is below ~0.8. And the fine aerosols begin to dominate more when AOD exceeds 0.8. The results here are rather consistent with the ones in Yu et al. (2011), Qi et al. (2016), and Zheng et al. (2016). However, the figure here further reflects that both fine and coarse particles themselves could cause very serious haze pollutions in YRD, leading to considerably high peaking values in both fine and coarse modes being found. This has not been observed in previous publications. The aerosol size distributions here are also very useful for optimizing numerical models. A more precise aerosol size distribution would make the models more accurate in describing the aerosol transportation, deposition as well as its radiative effects (Ma et al., 2017) in YRD or east China.

Figure 7

To further investigate the physical features, the seasonal variations of the aerosol effective and mean radius, as well as volume concentrations in urNJ are further presented in Figure 8. The mean effective radius, which is generally smaller than the mean one in all modes, is about 0.34, 0.16, and 2.18 μm for the total, fine and coarse aerosols, respectively, during the study period. It additionally reflects that the aerosols in urNJ are dominated by the fine particles as discussed previously. The seasonal variations of the radiuses have a good anti-correlation to the one of AEs (Figure 2). Both fine and coarse aerosol radius are larger in summer than in the other seasons due to the moisture absorption growth of the aerosols. However, the total aerosol radius is much larger in spring due to a larger coarse fraction. Different from the radius, the seasonal variations of the volume concentrations between fine

and coarse aerosols are different, peaking in spring for coarse aerosol while in summer for fine aerosol. Although both the fine and coarse aerosols have the same volume levels in urNJ annually, their contributions to the total aerosol volumes vary significantly with seasons. The coarse aerosol directly leads to the largest volume peaking in spring for the total aerosols.

Figure 8

3.3 Aerosol classification based on its optical properties

The aerosol clusters, to a certain degree, could be identified based on the relationships between SSA at 491 nm and AE at 491/870 nm, between real refractive index (RRI) at 670 nm and AE at 491/870 nm, as well as between SSA differences ($dSSA=SSA_{870nm}-SSA_{491nm}$) and AE at 491/870 nm as presented in Russell et al. (2014), who proposed a Mahalanobis Classification based on "a priori" information for each type aerosol source (e.g.: dust, urban, biomass aerosols). Different aerosols then would mostly concentrate within the corresponding ellipses of a two-dimensional scatter plot of SSA versus AE (or RRI versus AE, or dSSA versus AE). Based on their classification, the pure dust, polluted dust, biomass-burning, industrial urban, developing urban, marine aerosols (Figure 8 in Russell et al., 2014) all could be identified. For example: 1. The polluted dust aerosols would be mostly within the ellipses with smaller AE (near 1.0), relatively smaller SSA levels (0.85 to 0.95), but much larger real refractive index (1.45 to 1.55) and SSA differences (0 to 0.05) compared with other aerosols. 2. The aerosols from the developing urban generally have smaller sizes than the polluted dust (AE ranging from 1 to 1.6), but they have larger SSA (0.9 to 1.0), smaller real refractive index (1.4 to 1.5) and SSA differences (around 0). 3. The aerosols from the urban dominated by Industrial (UrbInd) or from

biomass burning have the largest AE (exceeding 1.6). However, the UrbInd aerosols have much larger SSA and SSA differences while smaller real refractive index compared with biomass burning aerosols. Based on their classification standards, aerosols in urNJ could basically be identified as the clusters of polluted dust, developing and industrial urban kinds during the sampling period as shown in Figure 9, which further supports the analysis in previous sections (Section 3). In spring, dusts emitted from the desert regions in northern or north of China could be transported in long distant arriving to YRD. During the transportation, trace gases or particles could be absorbed and then a heterogeneous chemical reaction occurs. And in other seasons, the aerosols are mostly from the local emissions within the urban areas and industrial areas around. Although urNJ is only about 300-400 km far away from the East China Sea, its aerosols are few composed by marine or sea salt components as illustrated in Figure 9. It is a pity that the observations missed a biomass burning event in Jun 2012 (Zhuang et al., 2014b, 2015) when the instrument was maintained. Otherwise, the figure will be more comprehensive. It's a very serious biomass burning episode, which directly results in extremely high BC surface concentrations (6-7 times to the annual means, Zhuang et al., 2014b). Analysis here might further help us to understand the aerosol sources, transformations, transports and its radiative effects in YRD. And it also indicates that the Mahalanobis Classification is a very useful approach for classifying the aerosol into types, especially in the cases of shortage of data or insufficient of methods. However, the method still has a limitation. The classified ellipses have some overlaps among different aerosols clusters. In overlap regions, it’s hard to further identify the aerosol into types. For example, it’s not easy to distinguish the polluted dust aerosol with large AE from the urban aerosols with smaller AE. Therefore, if there were two kinds of aerosols having nearly identical coordinates, further information is needed or more effective approaches should be taken into account.

Figure 9

In addition to the types, the aerosol mixtures/compositions could also be identified based on SSA and AAOD. Generally, dust aerosol has strong absorptions in ultraviolet (UV) band, but become non-absorbing in the visible band, leading to its SSAs increasing with wavelength monotonically. For biomass burning aerosol, its SSA would decrease with wavelength monotonically. Non-monotonically variation in SSA with the wavelength might be due to the other type aerosol dominated mixtures as indicated by Li et al. (2015c), who then proposed two curvature parameters defined as the second derivative of the second-order polynomial fit of SSA and wavelength and the fit of AAOD and wavelength as shown in Eq. 4 and Eq. 5 to provide additional information on the aerosol compositions.

$$\ln(SSA_\lambda) = \beta_2 \ln(\lambda)^2 + \beta_1 \ln(\lambda) + \beta_0 \quad (4)$$

$$\ln(AAOD_\lambda) = \alpha_2 \ln(\lambda)^2 + \alpha_1 \ln(\lambda) + \alpha_0 \quad (5)$$

Where, $-\beta_2$ and α_2 are the SSA Curvature and AADO Curvature, respectively. Detailed statements could be found in Li et al. (2015c). Based on these parameters, the aerosols could basically be identified as the dust dominated, black carbon (including biomass burning and urban/industrial aerosols) dominated and other mixed (peak) type aerosols, because the curvature probability (or frequency) distributions are different among different aerosol mixtures. As indicated in Li et al. (2015c), the SSA or AAOD Curvature is mostly concentrated at or around 0 for the BC dominated aerosol mixture, which is much smaller than that of dust dominated aerosol mixtures (0.1 for SSA Curvature and 0.5-1 for AAOD Curvature) over East Asia. Based on their method, the curvatures of SSA and AAOD are calculated and then divided into three categories according to the monotonicity of SSA.

Results show that there are about 15.0%, 27.5% and 42.3% occurrences of monotonically increasing, decreasing and 670 nm peaking SSA spectrums, respectively, in urNJ. And their probability (or frequency) distributions are plotted in Figure 10. Both SSA and AAOD Curvatures have substantial seasonality, larger in colder seasons (not shown here). The figure indicates that the SSA and AAOD curvature patterns are highly consistent with those in Li et al. (2015c) for the monotonic categories, which implying that there might be about 15% (mostly appearing in spring) and 27% (mostly being in fall and winter) occurrence of dust dominated and BC dominated mixing aerosols, respectively, in urNJ during the observed period. For example, a very strong dust storm from northwest China and Mongolia (Li et al., 2015a) directly yielded mean SSA and AAOD Curvatures of 0.12 and 1.11, respectively, on 1st May 2011, which are close to the values (0.11 and 1.24, respectively) of the pure dust aerosol (Li et al., 2015c). For the rest category with non-monotonic SSA spectrum, the SSA curvature are mostly concentrated from 0.3 to 0.8, implying that dust component might not exceed 10% while the scattering species (organic carbon not included) at least accounting for 30% within the mixing particle in west YRD according to the sensitive results in Li et al. (2015c). Subsidiary data are needed if more information were going to be further identified. Results here might help us to better understand the mixings of the aerosols in urban areas of YRD. Similar to the Russell et al. (2014), Li et al. (2015c) also provides an effective approach to classify the aerosol compositions based on a single data set (such as the CE-318 retrievals).

Figure 10

3.4 The direct radiative forcing of the aerosols

508 Basing on abovementioned wavelength dependent optical properties and combining with the
509 observed surface albedo and aerosol profiles, the clear sky size fractional aerosol direct radiative
510 forcing (DRF) of different components at both the top of atmosphere (TOA) and surface in urNJ are
511 investigated using a radiation transfer model TUV (Madronich, 1993). Due to lacking SSA
512 observations of each aerosol component, the scattering aerosol DRF is estimated based on a given SSA
513 value (0.9999, equaling to that of sulfate or nitrate aerosol) in reference (Li et al., 2015b). As indicated
514 in last section, absorbing aerosols in urNJ are always in a mixed state. Therefore, the absorbing aerosol
515 DRF is inappropriate to be estimated directly using the BC SSA. Here, it is derived from the difference
516 between the total and scattering aerosol DRFs, which might be more representativeness. To make
517 comparison, the aerosol DRF is also calculated based on AAODs, AAEs and black carbon (BC) SSA
518 (Li et al., 2015b).

519 Observed aerosol profiles, which have not been used in previous investigation (e.g.: Zhuang et al.,
520 2014a), might be important to the DRFs estimating. Figure 11 shows the mean vertical aerosol profiles
521 observed by CALIPSO (annual scale data) and Polarization-Raman Lidar (PRL, seasonal scale data) in
522 Nanjing. To make a comparison, all profiles in the figure have been standardized to the percentage (%).
523 Similar to AODs and AEs, the figure suggests that the ground and satellite based aerosol profiles also
524 exist substantial differences. The CALIPSO profile is more homogeneous than the PRL one,
525 accounting for about 61% and 88%, respectively, below 4 km. Due to lacking long-term measurement
526 of PRL and the different products among different observation platforms, both the CALIPSO and PRL
527 profiles are used here. Additionally, a combined profile (gray line) simply averaged between CALIPSO
528 and PRL is included. It indicates that aerosols account for about 75% of the totals below 4 km and
529 about 60% in the boundary layer for the combined profile, which to some extent is similar to the

530 default profile of TUV (Palancar and Toselli, 2004). The aerosol DRFs would be estimated by TUV
531 using all these four profiles.
532
533 Figure 11
534
535 **3.4.1 The aerosol direct radiative forcing in clear sky condition**
536 DRFs, unless otherwise specified, hereinafter all represent the averaged values among CALIPSO,
537 PRL and combined profile based forcing in clear sky condition. Figure 12 shows the seasonal
538 variations of the size fractional daytime TOA and surface DRFs of the total, scattering and absorbing
539 aerosols in urNJ. The aerosol DRFs are highly depended on the aerosol optical properties and
540 compositions. Overall, the fine aerosols have much more contributions to the total aerosol DRFs,
541 especially for scattering aerosols. The coarse aerosol DRF is only ~15% of the fine aerosol DRF for
542 scattering aerosols while >51% for absorbing aerosols at both the TOA and surface in urNJ. Negative
543 scattering aerosol DRFs could be significantly offset at the TOA while further strengthened at the
544 surface by absorbing aerosols. Therefore, the total coarse aerosol DRF at the TOA is very weak due to
545 a much smaller CSSA and subsequently it has a much smaller contribution to the total aerosol DRF
546 than the fine aerosols. Both the scattering and absorbing aerosol DRFs have similar seasonality to their
547 AODs, peaking in summer for the total scattering aerosols while in spring for the total absorbing
548 aerosols. However, the DRF seasonal variation of each aerosol type is consistent with each other within
549 the same mode, all peaking in summer in fine mode while in spring in coarse mode. In addition to
550 AODs, surface albedo and the solar zenith angle also have influence on the variation of the aerosol
551 DRFs. As implied in Zhuang et al. (2014a), a brighter surface would yield a weaker negative DRF

552 while a stronger positive DRF in the condition with fixed AOD. The seasonal mean surface albedo
553 averaged from four wavelengths (440, 670, 870 and 1020 nm) is about 0.145, 0.170, 0.129, and 0.137
554 in spring, summer, fall, and winter, respectively. Therefore, the scattering aerosol DRF is stronger in
555 winter than in spring, although SAOD is lower in winter. Similarly, a stronger TOA DRF of the fine
556 absorbing aerosols in spring than in winter might be also related to higher surface albedo and solar
557 zenith angles, although their AAODs in winter are substantially higher. The weakest surface DRF
558 appears in spring for fine absorbing aerosols and in summer for coarse absorbing aerosols possibly due
559 to a higher surface albedo in this season.

560 Unlike the single aerosol type, the total aerosol DRFs are co-affected by both the scattering and
561 absorbing aerosols, meaning that the seasonal variation of the TOA DRF is additionally related to the
562 SSAs' seasonality. Thus, the strongest TOA DRF of the total fine aerosols appears in winter instead of
563 summer, and the total coarse aerosol DRFs are positive at TOA in summer. For all modes, the seasonal
564 variation of the total aerosol DRFs at TOA are more consistent with that of the fine mode. Compared
565 with the TOA DRFs of the total aerosols, the variations of surface DRFs are much more consistent with
566 those of corresponding AODs, strongest in summer for fine aerosols while in spring for coarse aerosols.
567 The total aerosol DRFs at the surface are the strongest in summer and weakest in fall.

568

569 Figure 12

570

571 To make comparison (Figure 13), absorbing aerosol DRFs based on observed AAOD, AAE and
572 fresh BC SSA (Li et al., 2015b) are also accessed (named as the second way). Although the absorbing
573 aerosol DRFs are estimated in different ways, they are highly correlated at both the TOA and surface as

574 shown in the figure. Apparently, the DRFs from the second method are much weaker than that from the
575 first one possibly due to the absorbing aerosol in urNJ being always in mixed state as analysis in
576 previous section or as indicated in Zhuang et al. (2015). Jacobson (2000) suggests that the aged (mixed)
577 absorbing aerosols have much stronger ability to absorb solar radiation, with a factor of two. Zhuang et
578 al. (2013a and 2013b) stated that the simulated regional mean TOA DRF of the mixed BC (+1.56 W/m^2)
579 over East Asia is about1.9 times to that of none mixed BC. And the ratio is about 1.73 in this study,
580 implying that the absorbing aerosol DRF from the first way is reasonable. Comparison here further
581 proves the importance of the mixing states to estimate the absorbing aerosol radiative effects.
582
583 Figure 13
584
585 Table 3 lists the annual mean size fractional DRFs of the total, scattering and absorbing aerosols at
586 both the TOA and surface in urNJ. The DRFs at the surface are all stronger than those at the TOA. The
587 mean DRFs are -10.69, -16.45, 5.76 W/m^2 at TOA and -25.54, -21.37 and -8.38 W/m^2 at the surface for
588 the total, scattering and absorbing aerosols, respectively. The TOA DRFs in fine mode are nearly an
589 order of magnitude stronger than those in coarse mode for the total and scattering aerosols. The DRFs
590 of the fine absorbing aerosols have the same orders of magnitude as, but stronger than those of the
591 coarse absorbing aerosols.
592 Table 3
593
594 Various studies on the aerosol DRFs have been carried out based on observations or numerical
595 models. Over all, the DRFs of urban aerosols are much stronger than those on the regional or global

596 scale. Forster et al. (2007) summarized the global mean clear sky DRFs of the total aerosols from
597 observations being -5.4 W/m^2. Zhuang et al. (2013a and 2013b) indicated a simulated clear sky DRFs
598 being -4.97 W/m^2 for total aerosols while +1.2 W/m^2 for BC over East Asia. On a sub-regional or urban
599 scale, observed based analysis showed that the total aerosol DRF always exceeded at least 10^1 W/m^2
600 (Markowicz et al., 2008; Khatri et al., 2009; Wang et al., 2009; Kuhlmann and Quaas, 2010; Alam et al.,
601 2011; Che et al., 2015c, and so on). Kuhlmann and Quaas (2010) showed that the total aerosol DRFs
602 was about -25 W/m^2 over Qinghai-Tibet Plateau. Che et al. (2014; 2015c) indicated that the daytime
603 total aerosol DRFs in northeast China was about -16.82 W/m^2 while exceeded -30 W/m^2 in both the
604 rural and urban areas of north China Plain in polluted episodes. Our results show that aerosols in urban
605 area of west YRD could also exert very strong DRF, as large as -25.5 W/m^2 at the surface. Apparently,
606 the DRFs here would have smaller uncertainties than that from simulations because of the use of
607 observations. Compared with the results in Zhuang et al. (2014a), DRFs here might be more precise
608 because: 1. the observed aerosol profiles have not been used; and 2. the absorbed DRFs (might be
609 underestimated) were calculated using fresh BC SSA in Zhuang et al. (2014a). This study further
610 investigates the size fractional (fine and coarse) DRFs of different aerosol components in urban areas
611 of west YRD, which is in favor of better understanding the acts of aerosols affecting solar short wave
612 radiation. And these issues have not been addressed in previous researches. The results here could also
613 be used to validate the numerical simulations to evaluate the model performance on the aerosol
614 radiative effects.
615
616 **3.4.2 Sensitivity of the aerosol direct radiative forcing to aerosol profiles**
617 Different aerosol profiles might result in different DRFs. Figure 14 presents the TOA and surface

618 DRFs of the different aerosol types, including the scattering, absorbing aerosols and the totals, based on
619 four kinds of aerosol profiles from CALIPSO, PRL, Combined CALIPSO and PRL shown in Figure 11
620 as well as the default one in TUV (Palancar and Toselli, 2004) in clear sky condition. The figure shows
621 that the aerosol DRFs in clear sky is not very sensitive to the aerosol profiles, although the absorbing
622 aerosol TOA-DRFs are more sensitive than scattering aerosols. Overall, both the scattering and
623 absorbing aerosol DRFs at TOA would become weaker to some extent if more aerosols were
624 concentrated in lower layers of atmosphere or within boundary layer especially for the latter one. Here,
625 a profile impact factor: PIF is defined as the ratio of the standard deviations among the four types of
626 DRFs in Figure 14 to the averaged values among these four DRFs. The PIF is about 4.97% for
627 absorbing aerosol TOA-DRF while below 2% for the rest types of DRFs, further proving the weak
628 influence of the aerosol profile on the clear sky DRFs. In contrast, the aerosol profiles might have
629 much more influence on the DRFs in cloudy sky condition because the absorbing aerosols over brighter
630 cloud would absorb more short wave radiation (Podgorny and Ramanathan, 2001). This issue is also
631 going to be addressed in the further.
632
633 Figure 14
634
635 **3.4.3 Briefly discussions**
636 Although the observation based DRFs of the total, scattering and absorbing aerosols, as well as
637 their sensitivities to the aerosol profiles are analyzed in this study; uncertainties still exist due to the
638 measurement errors of the optical properties mentioned in Section 2. Additional estimations of the
639 aerosol DRFs are carried out based on the errors of AOD, AAOD and SSAs. Results indicate that larger

uncertainties of the aerosol DRFs are mainly derived from the errors of SSA or AAOD. Uncertainty of total aerosol AOD (0.01) only yield about 1% relative bias for the total aerosol DRFs at both the TOA and surface. The total or fine aerosol SSA error (0.03 or 0.037) may result in about 24% uncertainties at the TOA (<15% at the surface) to the corresponding DRFs. A larger coarse aerosol SSA error (0.085) leads to a ~24% uncertainties of its surface DRFs. AAOD errors (0.01) cause about 20% uncertainties to the absorbing DRFs at both the TOA and surface, while only 1.2% to the scattering DRFs. Overall, these uncertainties are relatively smaller than those presented in 5th IPCC report (IPCC, 2013) and they could be further decreased if the measurements or the algorithms were further improved. In addition to the uncertainties, this study still exist limitations to be addressed in the future. First, the absorbing aerosol SSA should be further measured to better estimate corresponding DRFs. Second, the DRF would be a little more precise if the aerosols profiles with higher temporal resolutions were used instead of their annual means. Third, long-term trends of the aerosol optical properties and direct radiative forcing, including their interannual and interdecadal variations, should be taken into consideration. Finally, extremely high aerosol loadings are frequently observed in serious pollution episodes, including dust storms, biomass burning, and regional transport (Zhuang et al., 2014a, b and 2015). The aerosol optical and physical properties as well as the radiative forcing would be rather different in these extreme episodes, which also deserve further studies.

4 Conclusions

In this study, the size fractional aerosol optical and physical properties observed by Cimel sun photometer (CE-318), as well as corresponding direct radiative forcing (DRF) calculated by a radiation transfer model TUV based on observations in urban area of Nanjing (urNJ), west YRD, are

662 investigated.

663 In urban area of west YRD, the annual mean total aerosol AOD at 550 nm is 0.65, mostly
664 contributed by the scattering components (0.61). The absorption fraction is as small as about ~6.7%,
665 changing with the seasons. There are about 80% of aerosols distributing in fine mode in urNJ during
666 the sampling periods. The absorption fraction is about 4.6% in fine mode while 15.5% in coarse mode,
667 showing a very different compositions and absorption characteristics of these two kinds of aerosols.
668 Compared with the satellite retrievals, the aerosol optical properties here have much higher temporal
669 resolutions and products. Further analysis on the aerosol optical properties indicates that there might be
670 about 15% and 27% occurrence of dust dominated and BC dominated mixing aerosols, respectively, in
671 west YRD during the observed period.

672 The aerosols in west YRD have a two-mode lognormal pattern in volume size distribution peaking
673 at the radius of 0.148 and 2.94 μm in annual scale. Both the fine and coarse particles have the same
674 contribution to the totals at lower aerosol loadings (AOD<0.8). In higher AOD (>0.8) levels, the fine
675 aerosols are predominate. Results further indicate that the fine or coarse aerosol could individually
676 induce a very serious polluted episode in urban region of west YRD. Both the fine and coarse aerosols
677 have the same level of volume concentrations, although their radiuses differ by an order of magnitude.

678 The mean DRF of the total aerosols is -10.69 W/m^2 at the TOA and -25.54 W/m^2 at the surface, in
679 clear sky condition. The fine aerosol DRF accounts for more than 97% of the totals at the TOA.
680 Estimations on the size fractional DRF of each aerosol component indicate that the coarse aerosol DRF
681 is only ~15% of the fine one within scattering aerosols while >51% within absorbing aerosols at both
682 the TOA and surface in urNJ. The DRFs estimated for urNJ in this study are much stronger than their
683 regional or global means.

684 The size fractional aerosol optical, physical properties and DRFs have significant seasonality in
685 west YRD. The DRF variations of each aerosol type within the same mode are mostly consistent with
686 the variations of corresponding AODs, all peaking in summer for the fine aerosols while in spring for
687 the coarse ones. However, the variations of total aerosol DRF at the TOA are different from
688 corresponding AOD within the same size segment because negative DRFs of the scattering are always
689 offset by absorbing aerosol. Both the fine and coarse aerosols have the largest size and are the most
690 absorbing in summer, which are different from the whole mode aerosols (in spring).

691 The sensitivities of clear sky aerosol DRFs to the aerosol profiles are not significant, all smaller
692 than 5%. Overall, both scattering and absorbing aerosol DRFs at TOA would become a little weaker to
693 some extent if more aerosols were concentrated in lower layers of atmosphere, especially for the
694 absorbed DRF. Further investigation suggests that another uncertainty of the DRFs is from the
695 measuring errors of the aerosol optical properties. Larger biases are mainly from the errors of SSA and
696 AAOD.

697

698 **Acknowledgements:** This work was supported by the National Key Basic Research Development
699 Program of China (2017YFC0209803, 2014CB441203, 2016YFC0203303), the National Natural
700 Science Foundation of China (41675143, 91544230, 41621005), and a project Funded by the Priority
701 Academic Program Development of the Jiangsu Higher Education Institutions (PAPD). The authors
702 would like to thank all members in the AERC of Nanjing University for maintaining instruments.

703

704 **5 References**

705 Alam, K., Trautmann, T., and Blaschke, T.: Aerosol optical properties and radiative forcing over

706 mega-city Karachi. Atmos. Res. 101, 773-782, 2011.
707 Angström, A.: On the atmospheric transmission of sun radiation and on dust in the air, Geogr. Ann., 11,
708 156–166, 1929.
709 Arnott, W. P., Hamasha, K., Moosmuller, H., Sheridan, P. J., and Ogren, J. A.: Towards aerosol
710 light-absorption measurements with a 7-wavelength aethalometer: evaluation with a photoacoustic
711 instrument and 3-wavelength nephelometer, Aerosol Sci. Tech., 39, 17–29,
712 doi:10.1080/027868290901972, 2005.
713 Bellouin, N., Boucher, O., Tanré, D., and Dubovik, O.: Aerosol absorption over the clear-sky oceans
714 deduced from POLDER-1 and AERONET observations, Geophys. Res. Lett., 30, 1748,
715 doi:10.1029/2003GL017121, 2003.
716 Bergin, M. H., Cass, G. R., Xu, J., Fang, C., Zeng, L., Yu, T., Salmon, L. G., Kiang, C. S., Tang, X. Y.,
717 Zhang, Y. H., and Chameides, W. L.: Aerosol radiative, physical, and chemical properties in Beijing
718 during June 1999, J. Geophys. Res., 106 (D16), 17969–17980, 2001.
719 Cai, H. K., Zhou, R. J., Fu, Y. F., Zheng, Y. Y., and Wang, Y. J.: Cloud-aerosol lidar with or thogonal
720 polarization detection of aerosol optical properties after a crop burning case, Clim. Environ. Res.,
721 16, 469–478, 2011.
722 Che, H. Z., Zhang, X. Y., Xia, X., Goloub, P., Holben, B., Zhao, H., Wang, Y., Zhang, X. C., Wang, H.,
723 Blarel, L., Damiri, B., Zhang, R., Deng, X., Ma, Y., Wang, T., Geng, F., Qi, B., Zhu, J., Yu, J., Chen,
724 Q., and Shi, G..: Ground-based aerosol climatology of China: aerosol optical depths from the China
725 Aerosol Remote Sensing Network (CARSNET) 2002–2013, Atmos. Chem. Phys., 15, 7619–7652,
726 2015a.
727 Che, H. Z., Zhao, H. J., Wu, Y. F., Xia, X. A., Zhu, J., Wang, H., Wang, Y. Q., Sun, J. Y., Yu, J., Zhang,

728 X. Y., and Shi, G. Y.: Analyses of aerosol optical properties and direct radiative forcing over urban
729 and industrial regions in Northeast China, Meteorology and Atmospheric Physics, 127(3), 345-354,
730 doi:10.1007/s00703-015-0367-3, 2015c.
731 Che, H., Wang, Y., and Sun, J.: Aerosol optical properties at Mt. Waliguan observatory, China, Atmos.
732 Environ., 45, 6004–6009, 2011.
733 Che, H., Xia, X., Zhu, J., Li, Z., Dubovik, O., Holben, B., Goloub, P., Chen, H., Estelles, V.,
734 Cuevas-Agulló, E., Blarel, L., Wang, H., Zhao, H., Zhang, X., Wang, Y., Sun, J., Tao, R., Zhang, X.,
735 and Shi, G.: Column aerosol optical properties and aerosol radiative forcing during a serious
736 haze-fog month over North China Plain in 2013 based on ground-based sunphotometer
737 measurements, Atmos. Chem. Phys., 14, 2125–2138, doi:10.5194/acp-14-2125-2014, 2014.
738 Che, H., Xia, X., Zhu, J., Wang, H., Wang, Y., Sun, J., Zhang, X., and Shi, G.: Aerosol optical
739 properties under the condition of heavy haze over an urban site of Beijing, China, Environ. Sci.
740 Pollut. R., 22, 1043–1053, doi:10.1007/s11356-014-3415-5, 2015b.
741 Che, H.,Wang, Y., Sun, J., Zhang, X., Zhang, X., and Guo, J.: Variation of Aerosol Optical Properties
742 over the Taklimakan Desert in China, Aerosol Air Qual. Res., 13, 777–785, 2013.
743 Chiang, C. W., Chen, W. N., Liang, W. A., Das, S. K., and Nee, J. B.: Optical properties of tropospheric
744 aerosols based on measurements of lidar, sun-photometer, and visibility at Chung-Li (25^{o}N, 121^{o}E),
745 Atmos. Environ., 41, 4128-4137, doi:10.1016/j.atmosenv.2007.01.019, 2007.
746 Deng, J. J., Zhang, Y. R., Hong, Y. W., Xu, L. L., Chen, Y. T., Du, W. J., and Chen, J. S.: Optical
747 properties of $PM_{2.5}$ and the impacts of chemical compositions in the coastal city Xiamen in China,
748 Science of the Total Environment, 557-558, 665-675, 2016.
749 Dubovik, O. and King, M. D.: A flexible inversion algorithm for the retrieval of aerosol optical

properties from Sun and sky radiance measurements, J. Geophys. Res., 105, 20673–20696, doi:10.1029/2000JD900282, 2000.

Dubovik, O., Sinyuk, A., Lapyonok, T., Holben, B. N., Mishchenko, M., Yang, P., Eck, T. F., Volten, H., Munoz, O., Veihelmann, B., van der Zande, W. J., Leon, J. F., Sorokin, M., and Slutsker, I.: Application of spheroid models to account for aerosol particle nonsphericity in remote sensing of desert dust, J. Geophys. Res.-Atmos., 111, D11208, doi:10.1029/2005jd006619, 2006.

Fan, X. H., Chen, H. B., Xia, X. A., Li, Z. Q., and Cribb, M.: Aerosol optical properties from the Atmospheric Radiation Measurement Mobile Facility at Shouxian. China, J. Geophys. Res., 115, D00K33, doi:10.1029/2010JD014650, 2010.

Forster, P., Ramaswamy, V., Artaxo, P., Berntsen, T., Betts, R., Fahey, D. W., Haywood, J., Lean, J., Lowe, D. C., Myhre, G., Nganga, J., Prinn, R., Raga, G., Schulz, M., and Van Dorland, R.: Changes in atmospheric constituents and in radiative forcing, in: Climate Change 2007: The Physical Science Basis. Contribution of Working Group I to the Fourth Assessment Report of the Intergovernmental Panel on Climate Change, edited by: Solomon, S. et al., Cambridge Univ. Press, Cambridge, UK, 129–234, 2007.

Hansen, A. D. A., Rosen, H., and Novakov, T.: The aethalometer: an instrument for the real time measurements of optical absorption by aerosol particles, Sci. Total Environ., 36, 191–196, 1984.

He, X., Li, C. C., Lau, A. K. H., Deng, Z. Z., Mao, J. T., Wang, M. H., and Liu, X. Y.: An intensive study of aerosol optical properties in Beijing urban area, Atmos. Chem. Phys., 9, 8903–8915, doi:10.5194/acp-9-8903-2009, 2009.

Holben, B. N., Eck, T. F., Slutsker, I., Tanre, D., Buis, J. P., Setzer, A., Vermote, E., Reagan, J. A., Kaufman, Y. J., Nakajima, T., Lavenu, F., Jankowiak, I., and Smirnov, A.: AERONET-a federated

772 instrument network and data archive for aerosol characterization, Remote Sens. Environ., 66, 1-16,
773 1998.
774 Holler, R., Ito, K., Tohno, S., and Kasahara, M.: Wavelength-dependent aerosol single scattering albedo:
775 measurements and model calculations for a coastal site near the sea of Japan during ACE-Asia, J.
776 Geophys. Res., 108, 8648, doi:10.1029/2002JD003250, 2003.
777 IPCC 2013: Climate Change 2013: The Physical Science Basis. Contribution of Working Group I to the
778 Fifth Assessment Report of the Intergovernmental Panel on Climate Change, edited by: Stocker, T.
779 F., Qin, D., Plattner, G.-K., Tignor, M., Allen, S. K., Boschung, J., Nauels, A., Xia, Y., Bex, V., and
780 Midgley, P. M., Cambridge University Press, Cambridge, UK and New York, NY, USA, 1535 pp.,
781 2013.
782 Jacobson, M. Z.: A physically based treatment of elemental carbon optics: implication for global direct
783 forcing of aerosols, Geophys. Res. Lett., 27, 217-220, 2000.
784 Jacobson, M. Z.: Control of fossil-fuel particulate black carbon and organic matter, possibly the most
785 effective method of slowing global warming, J. Geophys. Res., 107, 4410,
786 doi:10.1029/2001JD001376, 2002.
787 Jiang, Z., Liu, Z., Wang, T., Schwartz, C. S., Lin, H.-C., and Jiang, F.: Probing into the impact of
788 3DVAR assimilation of surface PM_{10} observations over China using process analysis, J. Geophys.
789 Res. Atmos., 118, 6738–6749, doi:10.1002/jgrd.50495, 2013.
790 Khatri, P., Ishizaka, Y., and Takamura, T.: A study on aerosol optical properties in an urban atmosphere
791 of Nagoya, Japan. J. Meteorol. Soc. Jpn., 87 (1), 19-38, 2009.
792 Kiehl, J. T. and Briegleb, B. P.: The relative roles of sulfate aerosols and greenhouse gases in climate
793 forcing, Science, 260, 311–314, 1993.

794 Kuhlmann, J., and Quaas, J.: How can aerosols affect the Asian summer monsoon? Assessment during
795 three consecutive pre-monsoon seasons from CALIPSO satellite data, Atmos. Chem. Phys., 10,
796 4673-4688, doi:10.5194/acp-10-4673-2010, 2010.
797 Li, J., Carlson, B. E., and Lacis, A. A.: Using single-scattering albedo spectral curvature to characterize
798 East Asian aerosol mixtures, J. Geophys. Res. Atmos., 120, 2037–2052, 2015c.
799 Li, J., Wang, W.-C., Liao, H., and Chang, W. Y.: Past and future direct radiative forcing of nitrate
800 aerosol in East Asia, Theor. Appl. Climatol., 121, 445–458, 2015b.
801 Li, S., Wang, T. J., Xie, M., Han, Y., and Zhuang, B. L.: Observed aerosol optical depth and angstrom
802 exponent in urban area of Nanjing, China, Atmos. Environ., 123, 350-356,
803 doi:10.1016/j.atmosenv.2015.02.048, 2015a.
804 Liao, H. and Seinfeld, J. H.: Global impacts of gas-phase chemistry-aerosol interactions on direct
805 radiative forcing by anthropogenic aerosols and ozone, J. Geophys. Res., 110, D18208,
806 doi:10.1029/2005JD005907, 2005.
807 Ma, X. X., Liu, H. N., Liu, J., and Zhuang, B. L.: Sensitivity of climate effects of black carbon in China
808 to its size distributions, Atmospheric Research, 185, 118-130, 2017.
809 Ma, X., and Yu, F.: Effect of spectral dependent surface albedo on Saharan dust direct radiative forcing.
810 Geophys. Res. Lett. 39, L09808, 2012.Madronich, S.: UV radiation in the natural and perturbed
811 atmosphere, In: Tevini,M. (Ed.), UV-B Radiation and Ozone Depletion, Effects on Humans,
812 Animals, Plants, Microorganisms, and Materials, Lewis Publisher, Boca Raton, pp. 17-69, 1993.
813 Markowicz, K. M., Flatau, P. J., Remiszewska, J., Witek, M., Reid, E. A., Reid, J. S., Bucholtz, Z., and
814 Hilben, B.: Observations and modeling of the surface aerosol radiative forcing during UAE. J.
815 Atmos. Sci. 65, 2877-2891, 2008.

816 Menon, S., Hansen, J., Nazarenko, L., and Luo, Y. F.: Climate effects of black carbon aerosols in China
817 and India, Science, 297, 2250–2253, doi:10.1126/science.1075159, 2002.
818 Palancar, G.G., and Toselli, B. M.: Effects of meteorology and tropospheric aerosols on UV-B radiation:
819 a 4-year study. Atmos. Environ. 18, 2749-2757, 2004.
820 Pan, L, Che, H. Z., Geng, F. H., Xia, X. A., Wang, Y. Q., Zhu, C. Z., Chen, M., Gao, W., and Guo, J. P.:
821 Aerosol optical properties based on ground measurements over the Chinese Yangtze Delta Region,
822 Atmos. Environ., 44, 2587-2596, doi:10.1016/j.atmosenv.2010.04.013, 2010.
823 Peng, Z., Liu, Z. Q., Chen, D., and Ban, J. M: Improving PM2:5 forecast over China by the joint
824 adjustment of initial conditions and source emissions with an ensemble Kalman filter, Atmos. Chem.
825 Phys., 17, 4837–4855, 2017.
826 Penner, J. E., Andreae, M., Annegarn, H., Barrie, L., Feichter, J., Hegg, D., Jayaraman, A., Leaitch, R.,
827 Murphy, D., Nganga, J., and Pitari, G.: Aerosols, their direct and indirect effects, in: Climate
828 Change 2001: The Scientific Basis. Contribution of Working Group I to the Third Assessment
829 Report of the Intergovernmental Panel on Climate Change, edited by: Houghton, J. T. et al.,
830 Cambridge University Press, Cambridge, UK and New York, NY, USA, 289–348, 2001.
831 Podgorny, I. A., and Ramanathan, V.: A modeling study of the direct effect of aerosols over the
832 tropical Indian Ocean, J Geophys. Res. 106, D20, 24097–24105, 2001.
833 Qi, B., Hu, D. Y., Che, H. Z., Du, R. G., Wu, Y. F., Xia, X. A., Zha, B., Liu, J., Niu, Y. W., Wang, H.,
834 Zhang, X. Y., and Shi, G. Y.: Seasonal variation of aerosol optical properties in an urban site of the
835 Yangtze Delta Region of China. Aerosol Air Qual. Res., 16, 2884-2896, 2016.
836 Reddy, M. S., Boucher, O., Bellouin, N., Schulz, M., Balkanski, Y., Dufresne, J. L., and Pham, M.:
837 Estimates of global multicomponent aerosol optical depth and direct radiative perturbation in the

838 Laboratoire de Meteorologie Dynamique general circulation model, J. Geophys. Res., 110, D10S16,
839 doi:10.1029/2004JD004757, 2005.
840 Russell, P. B., Kacenelenbogen, M., Livingston, J. M., Hasekamp, O. P., Burton, S. P., Schuster, G. L.,
841 Johnson, M. S., Knobelspiesse, K. D., Redemann, J., Ramachandran, S., and Holben, B.: A
842 multiparameter aerosol classification method and its application to retrievals from spaceborne
843 polarimetry, J. Geophys. Res.-Atmos., 119, 9838–9863, doi:10.1002/2013JD021411, 2014.
844 Sun, H., Pan, Z., and Liu, X.: Numerical simulation of spatial-temporal distribution of dust aerosol and
845 its direct radiative effects on East Asian climate, J. Geophys. Res., 117, D13206,
846 doi:10.1029/2011JD017219, 2012.
847 Tao, R., Che, H. Z., Chen, Q. L., Tao, J., Wang, Y. Q., Sun, J. Y., Wang, H., and Zhang, X. X.: Study of
848 aerosol optical properties based on ground measurements over Sichuan Basin, China, Aerosol and
849 Air Quality Research, 14: 905–915. doi:10.4209/aaqr.2012.07.0200, 2014.
850 Wang, T. J., Zhuang, B. L., Li, S., Liu, J., Xie, M., Yin, C. Q., Zhang, Y., Yuan, C., Zhu, J. L., Ji, L. Q.,
851 and Han, Y.: The interactions between anthropogenic aerosols and the East Asian summer monsoon
852 using RegCCMS, J. Geophys. Res. Atmos., 120, doi:10.1002/2014JD022877, 2015.
853 Wang, Y., Che, H. Z., Ma, J. Z., Wang, Q., Shi, G. Y., Chen, H. B., Goloub, P., and Hao, X. J.: Aerosol
854 radiative forcing under clear, hazy, foggy, and dusty weather conditions over Beijing, China,
855 Geophys. Res. Lett., 36, L06804, doi:10.1029/2009GL037181, 2009.
856 Weingartner, E., Saathoff, H., Schnaiter, M., Streit, N., Bitnar, B., and Baltensperger, U.: Absorption of
857 light by soot particles: determination of the absorption coefficient by means of aethalometers, J.
858 Aerosol Sci., 34, 1445–1463, doi:10.1016/S0021-8502(03)00359-8, 2003.
859 Wu, Y. F., Zhang, R. J., Pu, Y. F., Zhang, L. M., Ho, K. F., and Fu, C. B.: Aerosol optical properties

observed at a semi-arid rural site in northeastern China, Aerosol Air Qual. Res., 12, 503–514, 2012.

Xia, X. A., Li, Z. Q., Holben, B., Wang, P., Eck, T., Chen, H. B., Cribb, M., and Zhao, Y. X.: Aerosol optical properties and radiative effects in the Yangtze Delta region of China, J. Geophys. Res., 112, D22S12, doi:10.1029/2007JD008859, 2007.

Xia, X., Che, H., Zhu, J., Chen, H., Cong, Z., Deng, X., Fan, X., Fu, Y., Goloub, P., Jiang, H., Liu, Q., Mai, B., Wang, P., Wu, Y., Zhang, J., Zhang, R., and Zhang, X.: Ground-based remote sensing of aerosol climatology in China: aerosol optical properties, direct radiative effect and is parameterization, Atmos. Environ., 214, 243-251, doi:10.1016/j.atmosenv.2015.06.071, 2016.

Xu, J., Bergin, M. H., Greenwald, R., Schauer, J. J., Shafer, M. M., Jaffrezo, J. L., and Aymoz, G.: Aerosol chemical, physical, and radiative characteristics near a desert source region of Northwest China during ACE-Asia, J. Geophys. Res., 109, D19S03, doi:10.1029/2003JD004239, 2004.

Xu, J., Bergin, M. H., Yu, X., Liu, G., Zhao, J., Carrico, C. M., and Baumann, K.: Measurement of aerosol chemical, physical and radiative properties in the Yangtze delta region of China, Atmos. Environ., 36, 161–173, 2002.

Xu, J., Tao, J., Zhang, R., Cheng, T., Leng, C., Chen, J., Huang, G., Li, X., and Zhu, Z.: Measurements of surface aerosol optical properties in winter of Shanghai, Atmos. Res., 109-110, 25–35, 2012.

Xu, X.: Retrieval of aerosol microphysical properties from AERONET photolarimetric measurements. PhD diss., Department of Earth and Atmospheric Sciences, University of Nebraska-Lincoln, 2015.

Yan, P., Tang, J., Huang, J., Mao, J. T., Zhou, X.J., Liu, Q., Wang, Z. F., and Zhou, H. G.: The measurement of aerosol optical properties at a rural site in Northern China, Atmos. Chem. Phys., 8, 2229–2242, doi:10.5194/acp-8-2229-2008, 2008.

Yu, J., Che, H. Z., Chen, Q. L., Xia, X. A., Zhao, H. J., Wang, H., Wang, Y. Q., Zhang, X. X., and Shi,

882 G. Y.: Investigation of aerosol optical depth (AOD) and Ångström exponent over the desert region
883 of northwestern China based on measurements from the China Aerosol Remote Sensing Network
884 (CARSNET), Aerosol Air Qual. Res., 15, 2024-2036, doi:10.4209/aaqr.2014.12.0326, 2015.
885 Yu, X. N., Ma, J., Kumar, K. R., Zhu, B., An, J. L., He, J. Q., and Li, M.: Measurement and analysis of
886 surface aerosol optical properties over urban Nanjing in the Chinese Yangtze River Delta, Sci. Total
887 Environ., 542, 277-291, 2016.
888 Yu, X. N., Zhu, B., Yin, Y., Fan, S. X., and Chen, A. J.: Seasonal variation of columnar aerosol optical
889 properties in Yangtze River Delta in China, Adv. Atmos. Sci., 28(6), 1326-1335,
890 doi:10.1007/s00376-011-0158-9, 2011.
891 Zhang, L., Sun, J. Y., Shen, X. J., Zhang, Y. M., Che, H., Ma, L. Q., Zhang, Y. W., Zhang, X. Y., and
892 Ogren, J. A.: Observations of relative humidity effects on aerosol light scattering in the Yangtze
893 River Delta of China, Atmos. Chem. Phys., 15, 8439–8454, 2015.
894 Zhang, Q., Streets, D. G., Carmichael, G. R., He, K. B., Huo, H., Kannari, A., Klimont, Z., Park, I. S.,
895 Reddy, S., Fu, J. S., Chen, D., Duan, L., Lei, Y., Wang, L. T., and Yao, Z. L.: Asian emissions in
896 2006 for the NASA INTEX-B mission, Atmos. Chem. Phys., 9, 5131–5153,
897 doi:10.5194/acp-9-5131-2009, 2009.
898 Zhang, W., Hu, B., Chen, C. H., Du, P., Zhang, L., and Feng, G. H.: Scattering properties of
899 atmospheric aerosols over Lanzhou City and applications using an integrating nephelometer, Adv.
900 Atmos. Sci., 21(6), 848–856, 2004.
901 Zhang, X. Y., Wang, Y. Q., Niu, T., Zhang, X. C., Gong, S. L., Zhang, Y. M., and Sun, J. Y.:
902 Atmospheric aerosol compositions in China: Spatial/temporal variability, chemical signature,
903 regional haze distribution and comparisons with global aerosols, Atmos. Chem. Phys., 12, 779–799,

904 doi:10.5194/acp-12-779-2012, 2012.

905 Zhao, H. J., Che, H. Z., Zhang, X. Y., Ma, Y. J., Wang, Y. F., Wang, X. X., Liu, C., Hou, B., and Che,
906 X. C.: Aerosol optical properties over urban and industrial region of Northeast China by using
907 ground-based sun-photometer Measurement, Atmos. Environ., 75, 270-278.
908 doi:10.1016/j.atmosenv.2013.04.048, 2013.

909 Zheng, Y., Che, H. Z., Zhao, T. L., Xia, X. A., Gui, K., An, L. C., Qi, B., Wang, H., Wang, Y. Q., Yu, J.,
910 and Zhang, X. Y.: Aerosol optical properties during the World Athletics Championships and Victory
911 Day Military Parade over Beijing in August and September 2015, Atmosphere, 7(3), 47;
912 doi:10.3390/ atmos7030047, 2016.

913 Zhu, J., Che, H. Z., Xia, X. A., Chen, H. B., Goloub, P., and Zhang, W. X.: Column-integrated aerosol
914 optical and physical properties at a regional background atmosphere in North China Plain, Atmos.
915 Environ., 84, 54-64, doi:10.1016/j.atmosenv.2013.11.019, 2014.

916 Zhu, J., Wang, T., Talbot, R., Mao, H., Hall, C. B., Yang, X., Fu, C., Zhuang, B., Li, S., Han, Y., and
917 Huang, X.: Characteristics of atmospheric Total Gaseous Mercury (TGM) observed in urban
918 Nanjing, China, Atmos. Chem. Phys., 12, 12103–12118, doi:10.5194/acp-12-12103-2012, 2012.

919 Zhuang, B. L., Li, S., Wang, T. J., Deng, J. J., Xie, M., Yin, C. Q., and Zhu, J. L.: Direct radiative
920 forcing and climate effects of anthropogenic aerosols with different mixing states over China,
921 Atmos. Environ., 79, 349–361, doi:10.1016/j.atmosenv.2013.07.004, 2013a.

922 Zhuang, B. L., Liu, Q., Wang, T. J., Yin, C. Q., Li, S., Xie, M., Jiang, F., and Mao, H. T.: Investigation
923 on semi-direct and indirect climate effects of fossil fuel black carbon aerosol over China, Theor.
924 Appl. Climatol., 114, 651–672, doi:10.1007/s00704-013-0862-8, 2013b.

925 Zhuang, B. L., Wang, T. J., Li, S., Liu, J., Talbot, R., Mao, H. T., Yang, X. Q., Fu, C. B., Yin, C. Q.,

Zhu, J. L., Che, H. Z., and Zhang, X. Y.: Optical properties and radiative forcing of urban aerosols in Nanjing, China, Atmos. Environ., 83, 43–52, 2014a.

Zhuang, B. L., Wang, T. J., Liu, J., Li, S., Xie, M., Han, Y., Chen, P. L., Hu, Q. D., Yang, X. Q., Fu, C. B., Zhu, J. L.: The surface aerosol optical properties in urban area of Nanjing, west Yangtze River Delta, China, Atmos. Chem. Phys., 17, 1143–1160, 2017.

Zhuang, B. L., Wang, T. J., Liu, J., Li, S., Xie, M., Yang, X. Q., Fu, C. B., Sun, J. N., Yin, C. Q., Liao, J. B., Zhu, J. L., and Zhang, Y.: Continuous measurement of black carbon aerosol in urban Nanjing of Yangtze River Delta, China, Atmos. Environ., 89, 415–424, 2014b.

Zhuang, B. L., Wang, T. J., Liu, J., Ma, Y., Yin, C. Q., Li, S., Xie, M., Han, Y., Zhu, J. L., Yang, X. Q., and Fu, C. B.: Absorption coefficient of urban aerosol in Nanjing, west Yangtze River Delta, China, Atmos. Chem. Phys., 15, 13633–13646, 2015.

Figure captions:

Figure 1. Monthly variations of the total (a), scattering (b), and absorbing (c) aerosol optical depths (AOD) at 550 nm, including the ratio of the AOD in fine or coarse mode to the AOD in all mode (line with triangle markers in green) in urban area of Nanjing. The 10th, 25th, median, 75th, 90th percentile values of the all mode AOD are presented as box plots. The monthly means of the all mode AODs are presented as cycle markers in gray.

Figure 2. Monthly variations of the total (a), scattering (b), and absorbing aerosol (c) Ångström exponents (AE) at 440/870 nm for the all, fine and coarse modes in urban area of Nanjing.

Figure 3. Monthly variations of the all, fine, and coarse mode aerosol single scattering albedo (SSA) at 550 nm (a) and the aerosol refractive indices at 440 nm (b) in urban area of Nanjing.

948 Figure 4. Frequency distributions of the size dependent AODs at 550 nm (a), AEs at 440/870 nm (b),
949 SSAs at 550 nm (c) as well as the real and imaginary parts at 440 nm (c) in urban area of Nanjing.
950 Figure 5. Comparisons between CE-318 and MODIS based AOD at 550 nm and between AE at
951 440/870 nm for CE-318 and at 412/470 nm for MODIS in Nanjing.
952 Figure 6. Comparisons between the absorbing aerosol optical depth (AAOD) at 550 nm from CE-318
953 and surface absorption coefficient (AAC) at 520 nm from AE-31 (a) and between the column AAE at
954 440/870 nm from CE-318 and surface AAE at 470/880 nm from AE-31 (b) in urban Nanjing.
955 Figure 7. The averaged aerosol volume size ($\mu m^3/\mu m^2$) distributions in different seasons (a) and in
956 different AOD levels in urban Nanjing.
957 Figure 8. Seasonal variations of the effective (a, μm) and mean (b, μm) radius of aerosols as well as the
958 aerosol volume concentrations (c, $\mu m^3/cm^3$) in the all, fine and coarse modes in urban Nanjing.
959 Figure 9. Relationships between the monthly mean values of 491 nm SSA and total Ångström exponent
960 (AE) at 491/870 nm (a), between the monthly mean values of the real refractive index at 670 nm and
961 AE at 491/870 nm (b), and between the monthly mean values of the SSA difference (870–491 nm) and
962 AE at 491/870 nm (c).
963 Figure 10. Distribution of the SSA and AAOD Curvatures in urban area of Nanjing under different
964 spectral SSA conditions, including monotonically decreasing, increasing SSA spectra and peaked SSA
965 spectra.
966 Figure 11. The aerosol vertical proportions (%) from CALIPSO, Polarization-Raman Lidar and their
967 average in Nanjing.
968 Figure 12. Seasonal variations of the clear sky aerosol direct radiative forcing (DRF, W/m^2) at both
969 TOA (a~c) and the surface (d~f). The DRFs of the total (a, d), scattering (b, e) and absorbing (c, f)

aerosols in the all, fine and coarse modes are all investigated in urban Nanjing.

Figure 13. Comparisons in the absorbing aerosol DRFs (W/m^2) between from BC SSA and from the total aerosol DRF minus the scattering one.

Figure 14. Sensitivities of the TOA and the surface aerosol DRFs (day time, W/m^2) to the different aerosol profiles in clear conditions, for the total, scattering and absorbing aerosols.

Tables:

Table 1 Statistical summary of the columnar aerosol optical properties in urban area of Nanjing

Factors	Max	Min	Mean±SD	Meadian
550 nm AOD	2.3208	0.2723	0.6494±0.2852	0.5912
550 nm FAOD	2.2216	0.1468	0.5257±0.2806	0.4479
550 nm CAOD	0.9891	0.0139	0.1237±0.1076	0.0858
550 nm SAOD	2.2744	0.2443	0.6059±0.2747	0.5492
550 nm FSAOD	2.1459	0.1435	0.5014±0.2713	0.4263
550 nm CSAOD	0.8842	0.0113	0.1045±0.0957	0.0705
550 nm AAOD	0.2304	0.0020	0.0435±0.0240	0.0421
550 nm FAAOD	0.1424	0.0005	0.0244±0.0175	0.0208
550 nm CAAOD	0.1163	0.0009	0.0192±0.0145	0.0156
440/870 nm AE	1.9100	0.3085	1.2045±0.2856	1.2436
440/870 nm FAE	2.3625	0.3565	1.7083±0.2979	1.7364
440/870 nm CAE	-0.0789	-0.3805	-0.1876±0.0430	-0.1898
440/870 nm SAE	1.9916	0.2958	1.1976±0.3085	1.2386
440/870 nm FSAE	2.3653	0.3463	1.7102±0.2980	1.7368
440/870 nm CSAE	-0.1048	-0.7111	-0.3838±0.1017	-0.3864
440/870 nm AAE	3.4619	0.1483	1.3237±0.4820	1.2587
440/870 nm FAAE	4.5118	0.2912	1.7521±0.6470	1.6516
440/870 nm CAAE	3.1264	-0.0844	0.8748±0.4589	0.8209
550 nm SSA	0.9959	0.8053	0.9297±0.0335	0.9305
550 nm FSSA	0.9974	0.8388	0.9524±0.0261	0.9549
550 nm CSSA	0.9835	0.5898	0.8208±0.0754	0.8225
440 nm Real part	1.6000	1.3300	1.4423±0.0638	1.4374
440 nm Imaginary part	0.0301	0.0005	0.0084±0.0047	0.0078

AOD: Aerosol optical depth
FAOD: Fine aerosol optical depth
CAOD: Coarse aerosol optical depth
SAOD: Scattering aerosol optical depth
FSAOD: Scattering aerosol optical depth in fine mode
CSAOD: Scattering aerosol optical depth in coarse mode
AAOD: Absorbing aerosol optical depth
FAAOD: Absorbing aerosol optical depth in fine mode
CAAOD: Absorbing aerosol optical depth in coarse mode
AE: Ångström exponent of total aerosols

FAE: Ångström exponent of fine aerosols
CAE: Ångström exponent of coarse aerosols
SAE: Ångström exponent of scattering aerosols
FSAE: Ångström exponent of scattering aerosols in fine mode
CSAE: Ångström exponent of scattering aerosols in coarse mode
AAE: Ångström exponent of absorbing aerosols
FAAE: Ångström exponent of absorbing aerosols in fine mode
CAAE: Ångström exponent of absorbing aerosols in coarse mode
SSA: Single scattering albedo of total aerosols
FSSA: Single scattering albedo of fine aerosols
CSSA: Single scattering albedo of coarse aerosols

Table 2 Seasonal mean±SD of the columnar aerosol optical properties in urban area of Nanjing

Factors	MAM	JJA	SON	DJF
550 nm AOD	0.6788±0.2919	0.7508±0.3749	0.5866±0.2447	0.6560±0.2976
550 nm FAOD	0.4739±0.2613	0.6798±0.3793	0.5149±0.2462	0.5687±0.2978
550 nm CAOD	0.2048±0.1356	0.0710±0.0599	0.0717±0.0346	0.0873±0.0685
550 nm SAOD	0.6284±0.2835	0.7031±0.3728	0.5495±0.2342	0.6157±0.2829
550 nm FSAOD	0.4529±0.2552	0.6463±0.3760	0.4901±0.2366	0.5428±0.2846
550 nm CSAOD	0.1756±0.1225	0.0568±0.0497	0.0593±0.0315	0.0728±0.0601
550 nm AAOD	0.0503±0.0208	0.0477±0.0307	0.0372±0.0200	0.0403±0.0271
550 nm FAAOD	0.0211±0.0125	0.0335±0.0212	0.0248±0.0157	0.0259±0.0211
550 nm CAAOD	0.0292±0.0165	0.0142±0.0137	0.0124±0.0066	0.0144±0.0111
440/870 nm AE	0.9915±0.2385	1.2174±0.2639	1.3744±0.1907	1.3134±0.2461
440/870 nm FAE	1.7474±0.2896	1.4701±0.3075	1.7408±0.2582	1.6935±0.3019
440/870 nm CAE	-0.1998±0.0352	-0.1699±0.0471	-0.1862±0.0424	-0.1807±0.0464
440/870 nm SAE	0.9812±0.2687	1.2733±0.2950	1.3824±0.2043	1.2956±0.2697
440/870 nm SFAE	1.7555±0.2862	1.5218±0.3397	1.7492±0.2545	1.6809±0.3039
440/870 nm SCAE	-0.3752±0.0743	-0.2815±0.0678	-0.3797±0.0991	-0.4016±0.1162
440/870 nm AAE	1.1885±0.4500	0.7971±0.2657	1.3290±0.4533	1.5007±0.4520
440/870 nm FAAE	1.7352±0.6059	0.9943±0.2672	1.6715±0.5970	1.8947±0.6545
440/870 nm CAAE	0.8542±0.4665	0.3771±0.2753	0.8312±0.4479	0.9798±0.4235
550 nm SSA	0.9204±0.0313	0.9241±0.0422	0.9348±0.0331	0.9378±0.0331
550 nm FSSA	0.9527±0.0237	0.9405±0.0356	0.9518±0.0253	0.9555±0.0265
550 nm CSSA	0.8340±0.0628	0.7868±0.0953	0.8115±0.0752	0.8211±0.0810
440 nm Real part	1.4647±0.0628	1.4075±0.0609	1.4252±0.0602	1.4404±0.0582
440 nm Imaginary part	0.0084±0.0040	0.0083±0.0052	0.0080±0.0044	0.0083±0.0053

Table 3. The annual mean aerosol direct radiative forcing (W/m^2) in urban area of Nanjing

Species	Clear sky	
	TOA	Surface
TA	-10.69±3.37	-25.54±2.83
FA	-11.17±3.09	-21.37±2.78
CA	-0.33±0.60	-6.15±2.90
SA	-16.45±2.81	-17.17±2.96
FSA	-15.08±3.18	-15.74±3.35
CSA	-2.31±1.18	-2.42±1.24

AA	5. 76±1.27	-8.38±1.56
FAA	3.91±0.95	-5.63±1.16
CAA	1.99±1.07	-3.73±1.71

TA: Total aerosols

FA: Fine aerosols

CA: Coarse aerosols

SA: All scattering aerosols

FSA: Scattering aerosols in fine mode

CSA: Scattering aerosols in coarse mode

AA: All absorbing aerosols' forcing

FAA: Fine absorbing aerosols' forcing

CAA: Coarse absorbing aerosols' forcing

Figures:

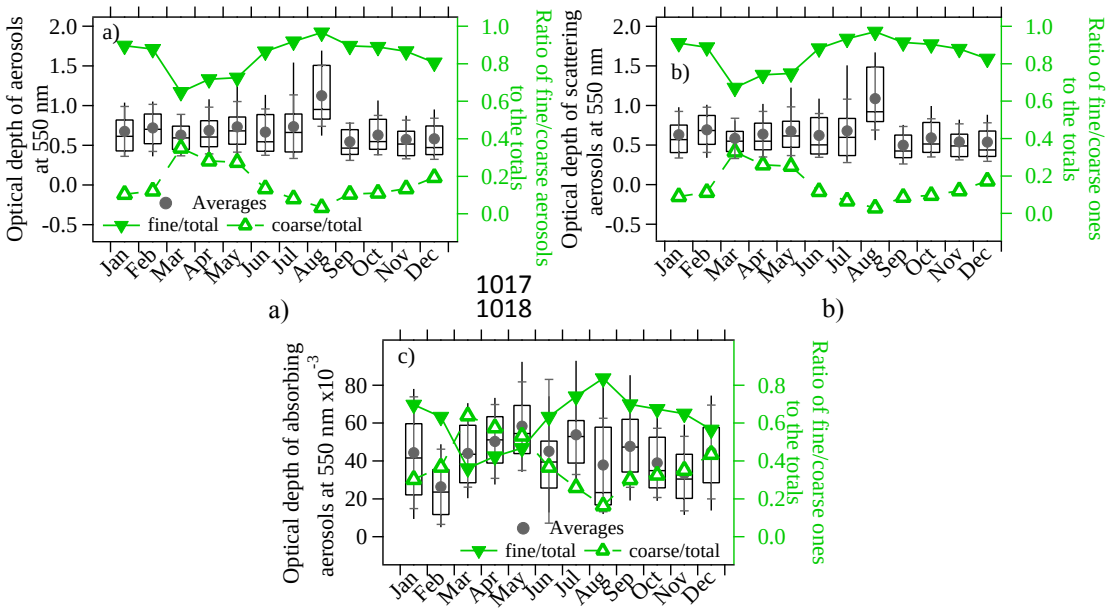

a) b)

c)

Figure 1.

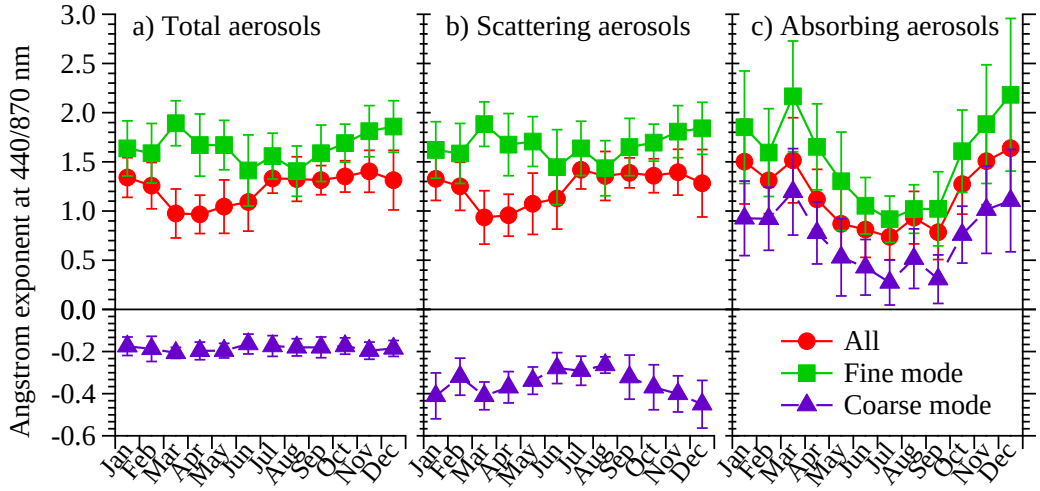

Figure 2.

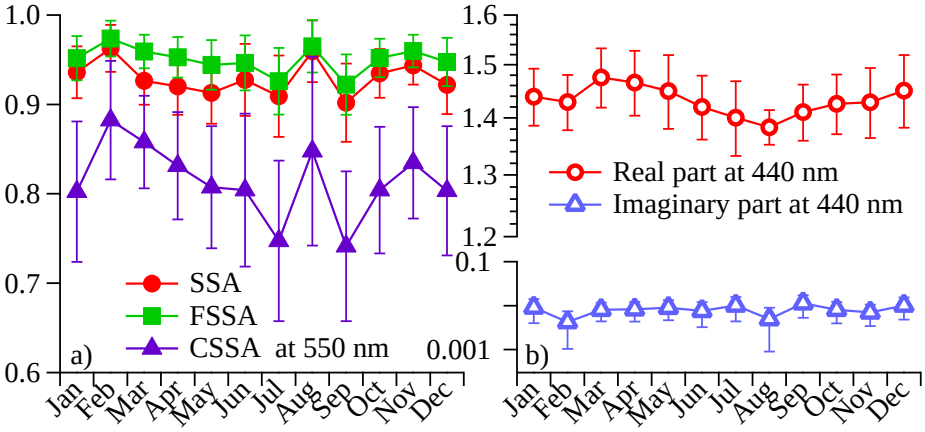

Figure 3

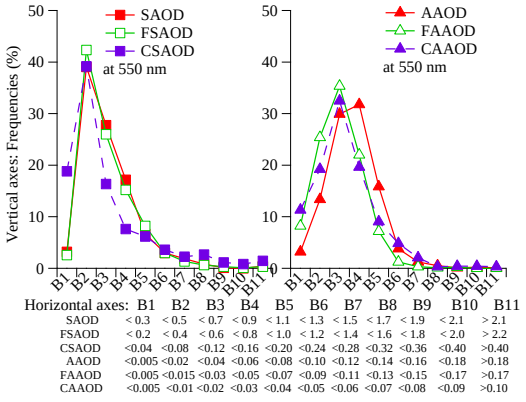

a)

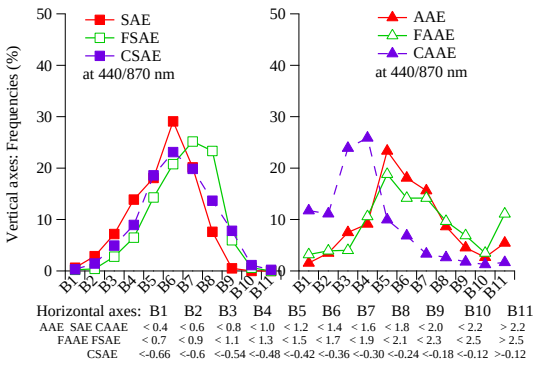

b)

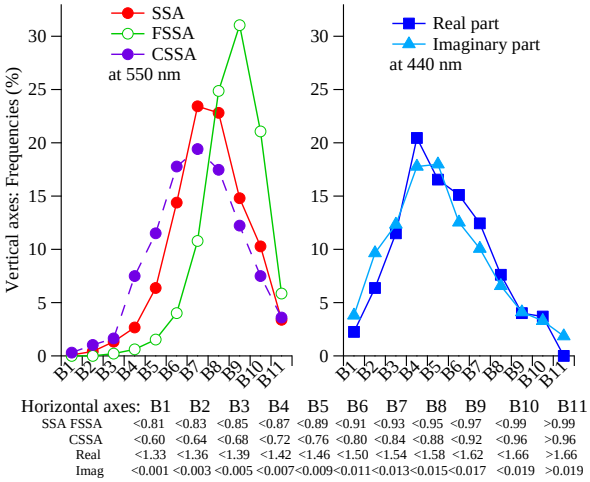

c)

Figure 4

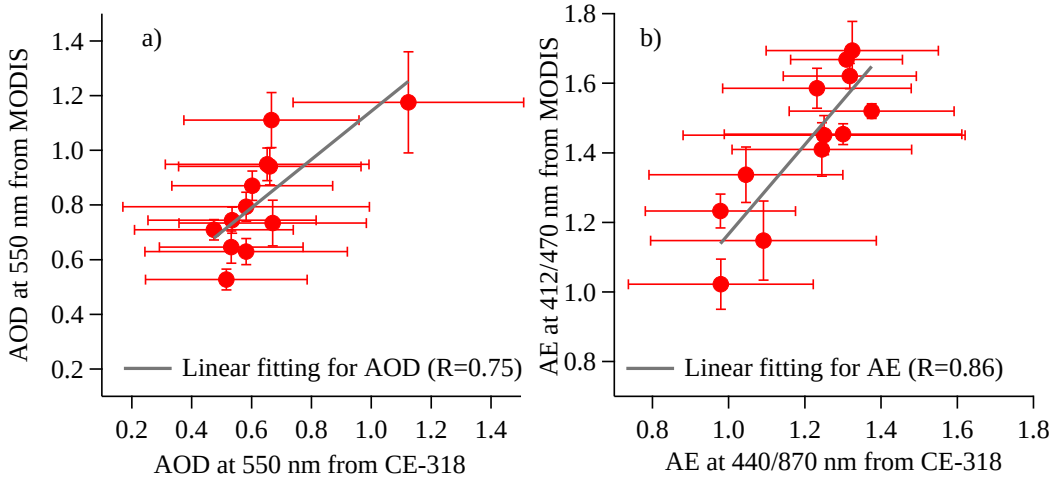

Figure 5

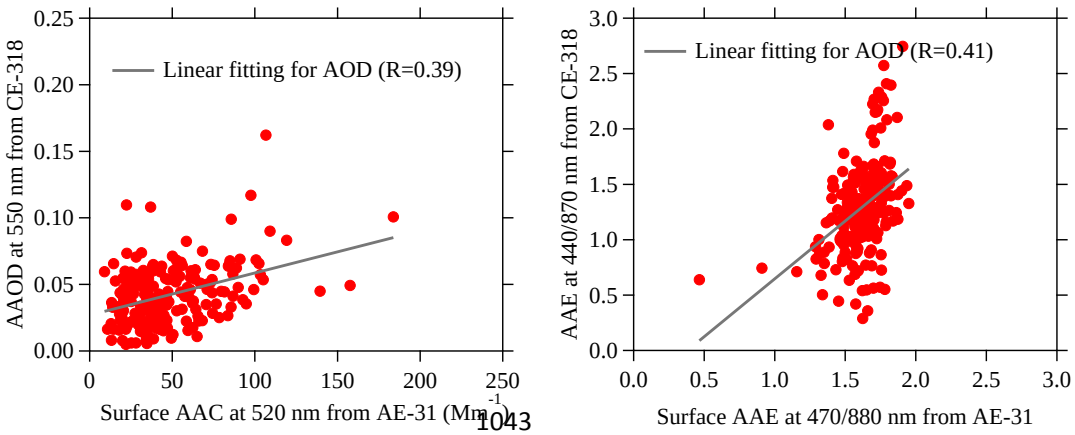

a) b)

Figure 6

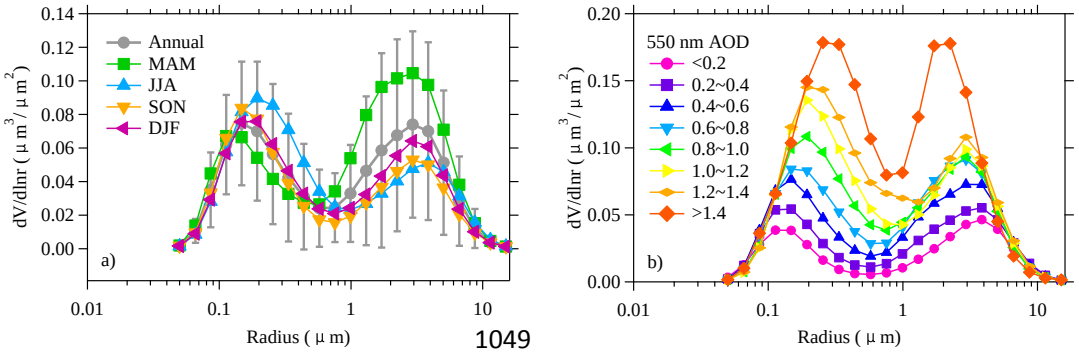

a) b)

Figure 7

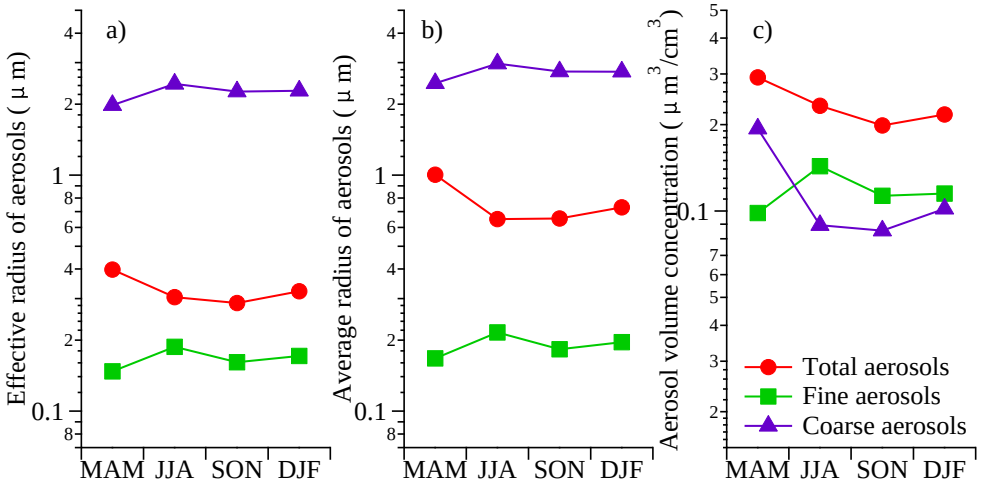

Horizontal axes: seasons

Figure 8

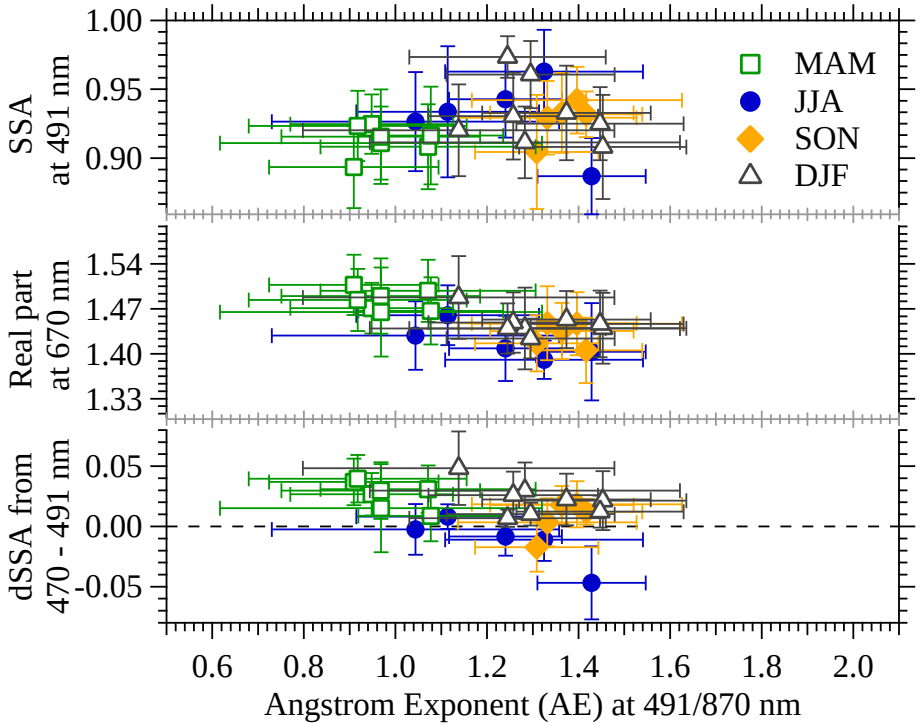

Figure 9

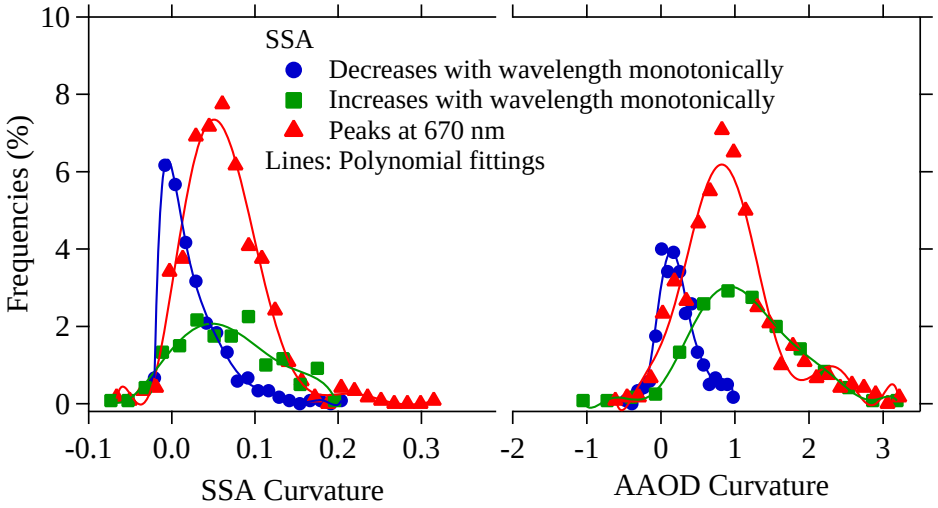

Figure 10

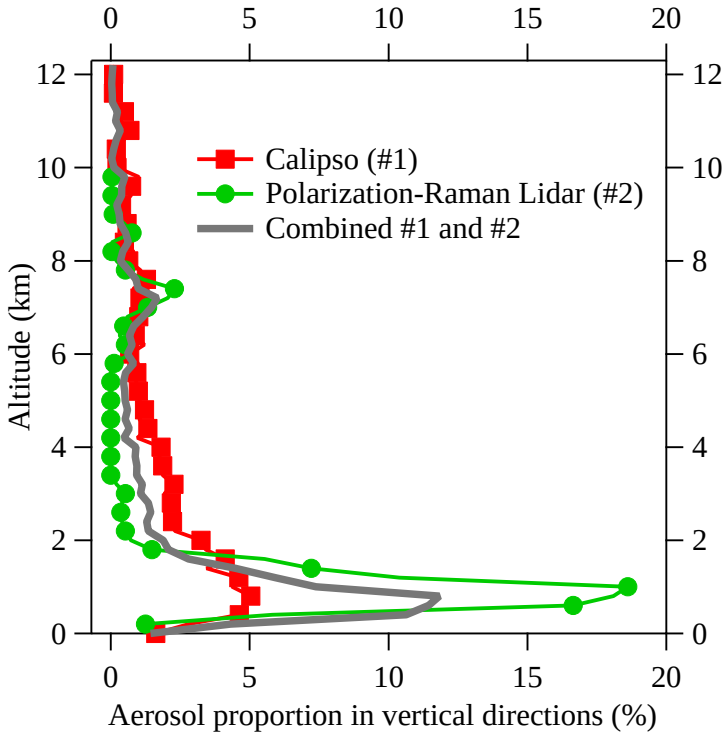

Figure 11

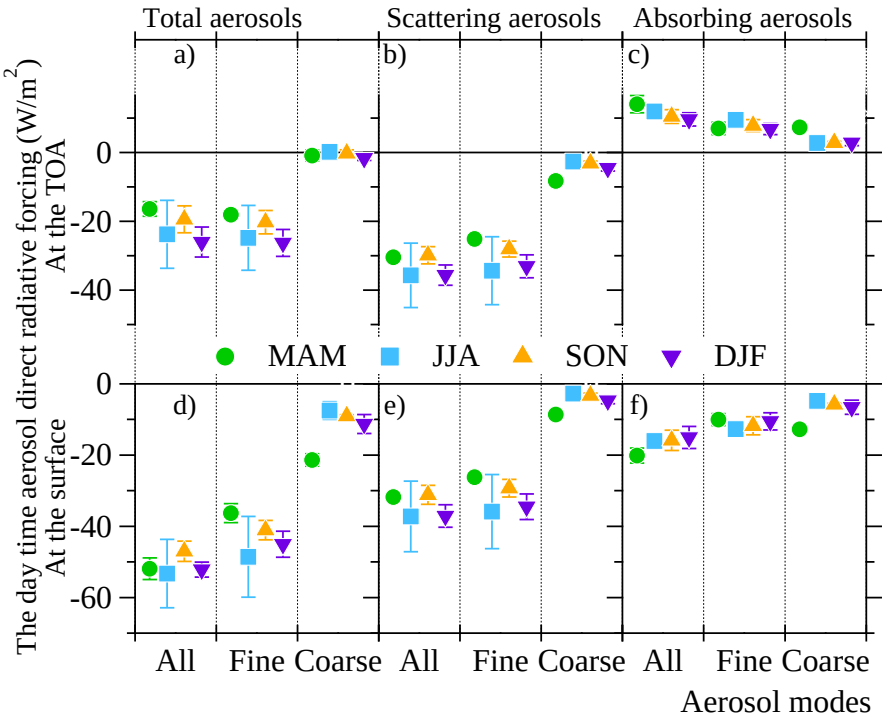

Figure 12

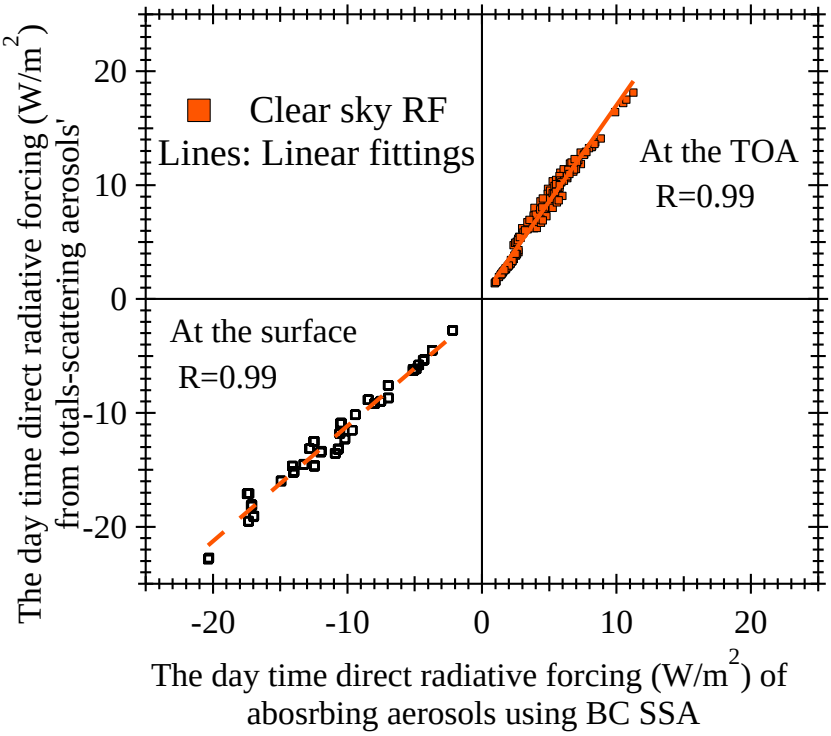

Figure 13

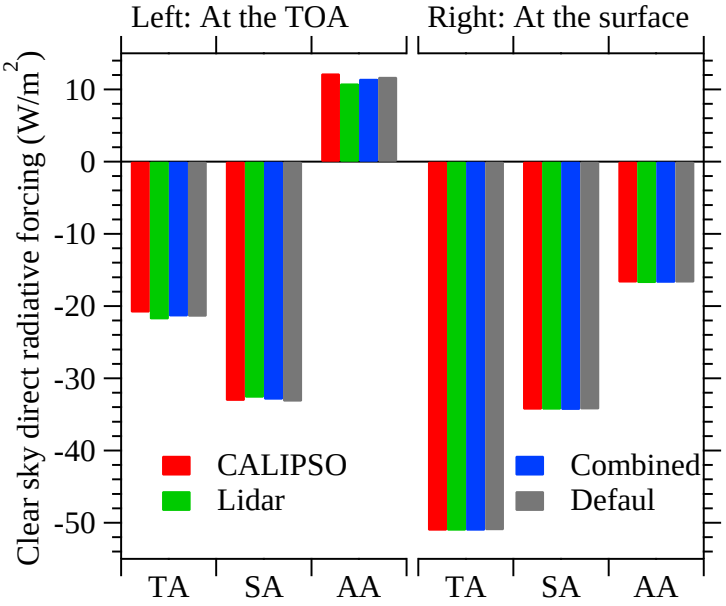

Figure 14